

# Magnetic evidence for a partially differentiated carbonaceous chondrite parent body

Laurent Carporzen<sup>a,1</sup>, Benjamin P. Weiss<sup>a,2</sup>, Linda T. Elkins-Tanton<sup>a</sup>, David L. Shuster<sup>b,c</sup>, Denton Ebel<sup>d</sup>, and Jérôme Gattacceca<sup>e</sup>

<sup>a</sup>Department of Earth, Atmospheric, and Planetary Sciences, Massachusetts Institute of Technology, Cambridge, MA 02139; <sup>b</sup>Berkeley Geochronology Center, Berkeley, CA 94709; <sup>c</sup>Department of Earth and Planetary Science, University of California, Berkeley, CA 94720; <sup>d</sup>Department of Earth and Planetary Sciences, American Museum of Natural History, New York, NY 10024; and <sup>e</sup>Centre Européen de Recherche et d'Enseignement des Géosciences de l'Environnement, Centre National de la Recherche Scientifique, Université Aix-Marseille 3, F-13545 Aix-en-Provence, France

Edited by David J. Stevenson, California Institute of Technology, Pasadena, CA, and approved February 22, 2011 (received for review November 23, 2010)

The textures of chondritic meteorites demonstrate that they are not the products of planetary melting processes. This has long been interpreted as evidence that chondrite parent bodies never experienced large-scale melting. As a result, the paleomagnetism of the CV carbonaceous chondrite Allende, most of which was acquired after accretion of the parent body, has been a long-standing mystery. The possibility of a core dynamo like that known for achondrite parent bodies has been discounted because chondrite parent bodies are assumed to be undifferentiated. Resolution of this conundrum requires a determination of the age and timescale over which Allende acquired its magnetization. Here, we report that Allende's magnetization was acquired over several million years (Ma) during metasomatism on the parent planetesimal in a  $> \sim 20 \mu\text{T}$  field up to approximately 9–10 Ma after solar system formation. This field was present too recently and directionally stable for too long to have been generated by the protoplanetary disk or young Sun. The field intensity is in the range expected for planetesimal core dynamos, suggesting that CV chondrites are derived from the outer, unmelted layer of a partially differentiated body with a convecting metallic core.

differentiation | planetesimal | magnetic field | early solar system | paleointensity

Allende is an accretionary breccia from near the surface of the CV parent planetesimal (1). Following accretion, Allende experienced minor aqueous alteration and moderate thermal metamorphism and metasomatism (2) but has remained essentially unshocked ( $< 5 \text{ GPa}$ ) (3). Its major ferromagnetic minerals are pyrrhotite, magnetite, and awaruite, with an average pseudo single-domain crystal size (4–8). We conducted alternating-field (AF) and thermal demagnetization, rock magnetic, and paleointensity measurements on 71 mutually oriented bulk subsamples of Allende sample AMNH5056 (approximately 10-cm diameter and 8-mm thick slab surrounded by fusion crust). Of these, 51 subsamples were taken from the interior of the meteorite ( $> 1 \text{ mm}$  from fusion crust), whereas 20 contained some fusion crust.

The differing magnetization directions of interior and fusion-crusted samples demonstrate that  $> 95\%$  of the natural remanent magnetization (NRM) in interior samples is preterrestrial (Figs. 1 and 2 and *SI Appendix*). AF demagnetization revealed that the interior samples have at least two components: a weak, low-coercivity, nonunidirectional component blocked up to 5 or 10 mT and a high-coercivity (HC) component blocked from approximately 10 to  $> 290 \text{ mT}$  (Fig. 1). In agreement with previous studies (4, 9, 10), the HC magnetization is unidirectionally oriented throughout the meteorite's interior (Fig. 2 and *SI Appendix*, Table S1). Thermal demagnetization (Figs. 1 and 2 and *SI Appendix*) indicates that interior samples have a low-temperature (LT) component blocked up to approximately  $190^\circ\text{C}$ , a dominant middle-temperature (MT) component blocked between approximately  $190\text{--}300^\circ\text{C}$  and oriented similarly to the

HC component isolated by AF demagnetization, and a very weak nonunidirectional high-temperature (HT) magnetization blocked up to approximately  $400\text{--}600^\circ\text{C}$ . The MT and LT components are each unidirectional throughout the meteorite and collectively constitute the majority (approximately 90%) of the interior NRM. Similar results were obtained by previous investigators (4, 5, 10). The HC component (Fig. 1) and its association with sulfide-rich separates demonstrates that it is carried predominantly by pyrrhotite (5, 11) (see *SI Appendix*). Blocking temperature relations and our magnetic viscosity experiments indicate that whereas the MT component should have been thermally stable at ambient temperatures over the last 4.5 billion years, the LT component may be a viscous remanent magnetization acquired in a strong (approximately  $500 \mu\text{T}$ ) crustal or fine-scale magnetostatic interaction field on the CV parent body (see *SI Appendix*). It is not clear whether the HT remanence is part of the meteorite's NRM or is instead simply an artifact of the laboratory demagnetization process (see *SI Appendix*).

The unidirectionality of the MT component requires that it was acquired following accretion of the CV parent body. This is consistent with the fact that the main NRM carriers (pyrrhotite, magnetite, and awaruite) are thought to be predominantly subsolidus alteration phases produced during hydrous alteration and thermal metamorphism on the parent body (2) (see *SI Appendix*). However, it has previously been unclear exactly how the MT component originated because its upper blocking temperature limit is close to pyrrhotite's  $\sim 320^\circ\text{C}$  Curie point: There have been differing conclusions (4, 10, 11) about whether it is a crystallization remanent magnetization (CRM) from low-temperature sulfidization or a partial thermoremanent magnetization (pTRM) acquired during metasomatism of the parent body. Our high-resolution thermal demagnetization schedule and laboratory TRM experiments strongly favor a  $290^\circ\text{C}$  pTRM (see *SI Appendix*). Additional strong evidence in favor of a pTRM or thermochemical remanence (TCRM) origin is provided by a variety of recently published petrologic constraints that indicate metamorphism to peak temperatures of approximately  $250$  to  $< 600^\circ\text{C}$  (see *SI Appendix*), essentially indistinguishable from the peak blocking temperature of the MT component.

Regardless of whether the MT component is a pTRM or TCRM, its unidirectional orientation—now observed by four

Author contributions: L.C. and B.P.W. designed research; L.C., L.T.E.-T., D.L.S., D.E., and J.G. performed research; D.L.S. and J.G. contributed new reagents/analytic tools; L.T.E.-T. provided theoretical context; L.C., B.P.W., D.E., and J.G. analyzed data; and L.C., B.P.W., D.L.S., and J.G. wrote the paper.

The authors declare no conflict of interest.

This article is a PNAS Direct Submission.

<sup>1</sup>Present address: Équipe de paléomagnétisme, Institut de Physique du Globe de Paris, Sorbonne Paris Cité, Université Paris Diderot, Centre National de la Recherche Scientifique, F-75005 Paris, France.

<sup>2</sup>To whom correspondence should be addressed. E-mail: bpweiss@mit.edu.

This article contains supporting information online at [www.pnas.org/lookup/suppl/doi:10.1073/pnas.1017165108/-DCSupplemental](http://www.pnas.org/lookup/suppl/doi:10.1073/pnas.1017165108/-DCSupplemental).

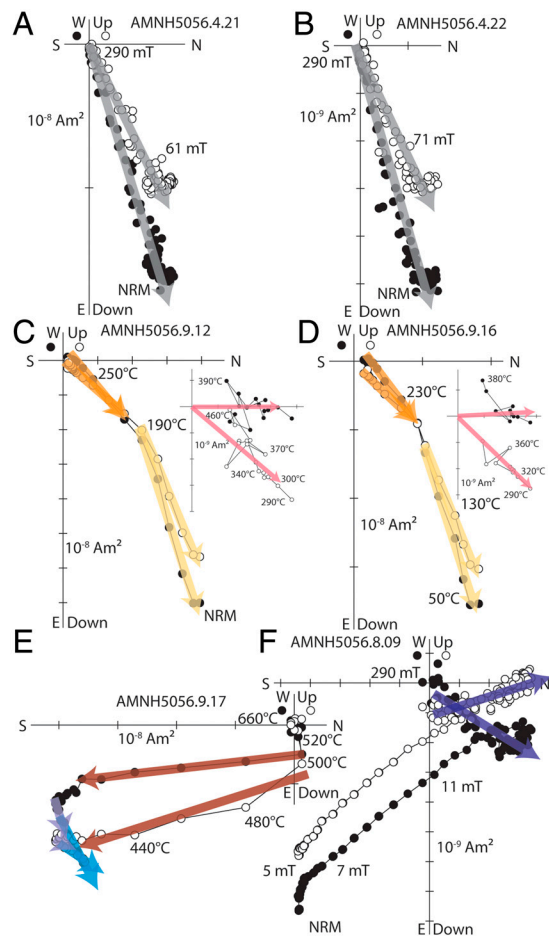


**Fig. 1.** AF and thermal demagnetization of Allende sample AMNH5056. Shown is a two-dimensional projection of the endpoint of the NRM vector during AF demagnetization. Closed and open symbols represent end points of magnetization projected onto horizontal (N-S-E-W) and vertical (U-D-E-W) planes, respectively. Peak fields for selected AF steps and peak temperatures for selected thermal steps are shown. (A and B) AF demagnetization of interior subsamples 4.21 and 4.22 reveals a dominantly single-component HC component (gray arrows). (C and D) Thermal demagnetization of interior subsamples 9.12 and 9.16 confirms that nearly all (>95%) of the remanence is composed of an LT component (blocked up to 190 °C; yellow arrows) and an MT component (blocked from 190–290 °C; orange arrows). *Insets* show the HT demagnetization steps that characterize the scattered HT remanence. (E) Thermal demagnetization of fusion-crusted sample 9.17. (F) AF demagnetization of fusion-crusted sample 8.09.

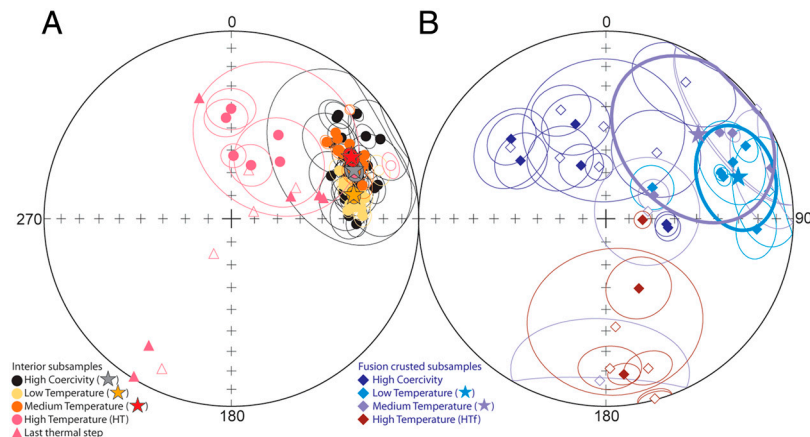


**Fig. 2.** Equal area plot showing directions of primary magnetization components of Allende subsamples from the interior (circle and triangles) (A) and fusion-crusted exterior (diamonds) (B). Solid symbols, lower hemisphere; open symbols, upper hemisphere. This plot is oriented in the same way as Fig. 1, with inclination = 90° oriented out of the page (perpendicular to the slab saw cut plane) and declination = 0° oriented toward the top of the page. Sample data ellipsoids are defined as maximum angular deviations associated with the least-squares fits. Stars and their ellipsoids represent the average directions and associated 95% confidence intervals (see *SI Appendix, Table S1*). Samples represented by triangles were only thermally demagnetized to 320 or 330 °C; the directions shown for these samples are the directions at this temperature (rather than a least-squares fit).

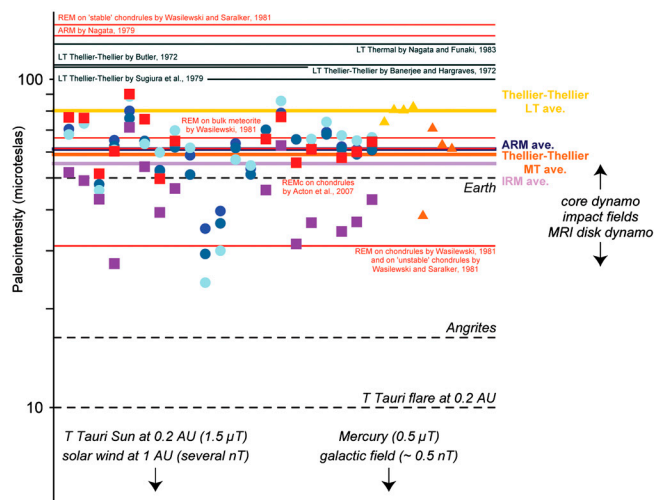


**Fig. 3.** Summary of paleointensities obtained for Allende. Each vertical cluster of points is derived from a single subsample in our study: circles, thermally calibrated anhysteretic remanent magnetization (ARM) paleointensities; squares, thermally calibrated IRM paleointensities; triangles, Thellier–Thellier paleointensities. Colors correspond to ARM bias fields of 50  $\mu$ T (light blue), 200  $\mu$ T (midblue), and 600  $\mu$ T (dark blue), IRM (red) and REM (purple), and LT (yellow) and MT (orange) paleointensities. Mean paleointensities from our ARM and IRM experiments (thermally calibrated from our measurements of ARM/TRM and IRM/TRM) are given by blue and purple lines, respectively. Mean paleointensities from our Thellier–Thellier experiments for the LT and MT components are given by the yellow and orange lines, respectively. For comparison, also shown in solid red and black lines are the mean previously measured paleointensities from Thellier–Thellier and AF (e.g., REM, REMc, ARM) methods, respectively (4–6, 9, 11, 25, 28, 29). REM and REMc are variants of the IRM paleointensity method (see ref. 6). We thermally calibrated the latter paleointensities also using our measurements of TRM/ARM and TRM/IRM. Shown for comparison are the surface fields of the Earth, the solar wind field 1 astronomical unit (AU) from the Sun, the galactic field, the inferred paleofields of a T Tauri short-lived flare at 0.2 AU, and surface fields inferred for the angrite parent body (12).

different laboratories (4, 9, 10)—combined with the lack of significant NRM blocked above 290 °C strongly argues against exotic scenarios like origin in a near-zero background field via magnetostatic interactions (which require preexisting strong NRM to produce such a directionally uniform component). We conducted paleointensity experiments using both Thellier–Thellier and AF-based (12) methods in order to obtain an order-of-magnitude estimate of the paleofields that produced the MT component (see *SI Appendix*). Our results indicate that it formed in fields of order 60  $\mu$ T with a minimum value of 20  $\mu$ T (Fig. 3

and *SI Appendix*). These strong paleointensities stringently constrain the origin and nature of the possible paleofield.

Several different geochronometers constrain the timing and duration of the magnetization acquisition. Pb/Pb (13) and Al/Mg (14) chronometry indicate that chondrules in CV chondrites formed over a period starting possibly within 0.2 Ma of calcium aluminum inclusion (CAI) formation and lasting for somewhere between 1.2–3 Ma (with most chondrules seeming to have formed approximately 1.7 Ma after CAIs) (see *SI Appendix*). Mn/Cr ages of secondary fayalite formed during aqueous alteration of six CV3 chondrites are approximately 5–8 Ma after CAIs (15) (see *SI Appendix*). Because aqueous alteration ended before or coincidentally with thermal metamorphism (16), the MT magnetization in Allende was acquired at or after these times. Most importantly, I/Xe ages of Allende CAIs (17) are younger than I/Xe ages of dark inclusions, refractory inclusions, and chondrules, and up to 9–10 Ma younger than the formation of CAIs (18). Assuming the I/Xe system records thermal disturbances, our I/Xe thermochronological modeling (Fig. 4 and *SI*

*Appendix*, Fig. S13) indicates that elevated thermal conditions (mean temperature of approximately 400 °C) lasted for several Ma ending at approximately 4,559 Ma. Such prolonged heating and cooling is consistent with a variety of other datasets. For example, the compositions of metal, sulfide, and oxide phases in Allende indicate prograde metamorphism at approximately 500 °C for  $>10^3$ – $10^4$  y (19).

Because chondrite parent bodies are assumed to be undifferentiated (20–23), the possibility of a core dynamo (24) has been discounted (6, 25–29) in support of early solar system external field sources. These ages indicate that the NRM in Allende is likely too young to have been produced by postulated early external field sources like the T Tauri Sun or the magnetorotational stability in the protoplanetary disk (30). Furthermore, the long (at least several Ma) duration of Allende metamorphism also would make it difficult for such field sources to produce a unidirectional magnetization in the spinning, orbiting CV parent body. Such a long timescale also precludes thermoremanent records of impact-generated fields [which should last  $<1$  d even

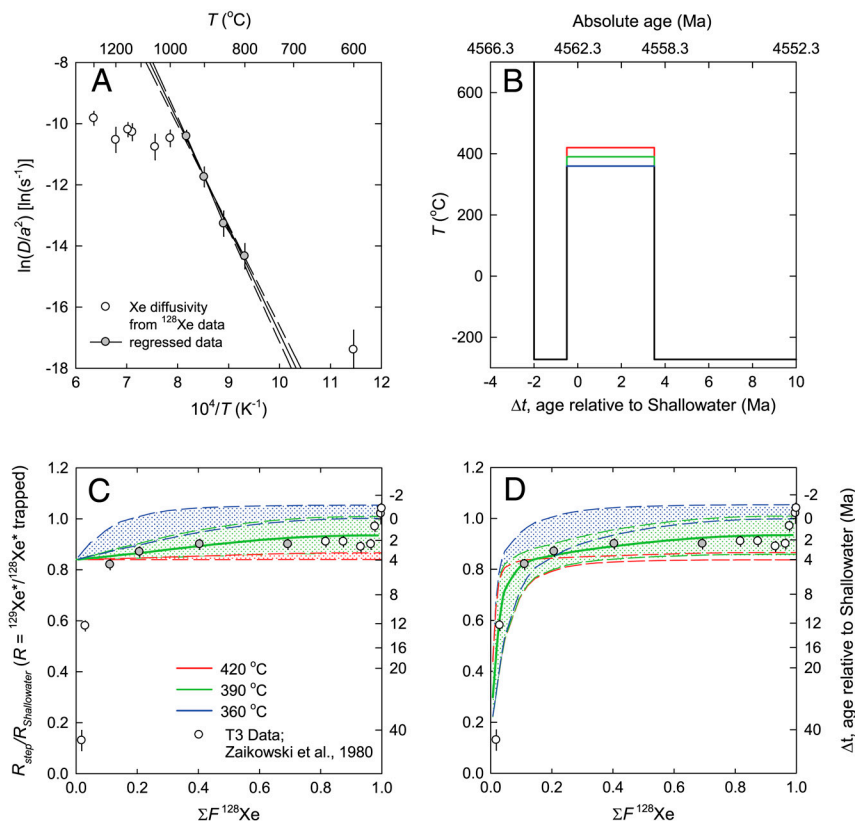


**Fig. 4.**  $^{129}\text{Xe}/^{128}\text{Xe}$  thermochronology of Allende CAI T3. These calculations use stepped degassing Xe data of ref. 17 (see *SI Appendix*). (A) Xe diffusivity as a function of temperature (Arrhenius plot). Points are diffusion coefficients calculated using measured  $^{128}\text{Xe}$  release fractions (see *SI Appendix*). The solid line is the model  $D(T)/a^2$  obtained from the linear regressions to approximately 50% of the  $^{128}\text{Xe}$  data (collected between 800 and 950 °C, indicated by gray points in A, C, and D) and used to calculate the curves shown in C and D; dashed lines indicate 1 $\sigma$  confidence interval on the regression. This regression corresponds to an activation energy ( $E_a$ ) for Xe diffusion =  $289 \pm 16$  kJ/mol and a frequency factor  $[\ln(D_0/a^2)] = 17.9 \pm 1.7[\ln(\text{s}^{-1})]$ .  $D(T)$  is the diffusivity of Xe as a function of temperature  $T$ , and  $a$  is the radius of the model diffusion domain. Extractions below 800 °C apparently sampled sites within the CAI with lower Xe retentivity, and the break in slope approximately 950 °C either reflects a phase transition during the analysis or a threshold temperature above which the analysis progressively sampled sites with higher Xe retentivity. (B) Simple thermal models tested against the Allende CAI  $^{129}\text{Xe}^*/^{128}\text{Xe}^*$  data shown as temperature ( $T$ ) plotted as a function of time relative to the I-Xe age of the Shallowater enstatite neutron fluence monitor (see *SI Appendix*). Positive (negative) values indicate time after (before) the I-Xe age of Shallowater. Present time would plot far off scale to the right. (C and D) Measured and modeled  $^{129}\text{Xe}^*/^{128}\text{Xe}^*$  ratio evolution spectra for the T3 CAI.  $^{129}\text{Xe}^*/^{128}\text{Xe}^*$  represents the radiogenic  $^{129}\text{Xe}$  component of each step after subtracting a common ordinary chondrite “OC-Xe” component (see *SI Appendix*). Circles are the  $^{129}\text{Xe}^*/^{128}\text{Xe}^*$  ratios of each step ( $R_{\text{step}}$ ) with associated uncertainties normalized to the ratio of Shallowater ( $R_{\text{Shallowater}}$ ) plotted versus the cumulative  $^{128}\text{Xe}$  release fraction ( $\Sigma F^{128}\text{Xe}$ ). Shown for reference on the right hand y axes of each plot are the apparent I-Xe ages of each step calculated relative to Shallowater. Also shown as curves in C are modeled release spectra using a spherical, one-domain model for the thermal histories shown in B. The curves in D are calculated using the same conditions as in C but also illustrate the effect of an additional phase with low Xe retentivity. Although the Xe diffusion kinetics for the lower retentivity site(s) is not well quantified (A), the young apparent age of the first step (approximately 40 Ma) indicates that the low retentivity sites did not quantitatively retain radiogenic  $^{129}\text{Xe}$  until that point in time or after. These calculations indicate that the apparent spatial distribution of radiogenic  $^{129}\text{Xe}$  within the Allende T3 CAI is well explained by an approximately 4 Ma long metamorphic event at a mean



for the largest impactors (31)]. Note that even if Allende had an LT (<25°C) CRM instead of TRM, the timescales of aqueous alteration [estimated to be approximately 1–10<sup>4</sup> y (32)] were likely still too long for recording these external field sources. Finally, the low ratio of NRM to saturation isothermal remanent magnetization (IRM) precludes nebular lightning as a field source.

Allende's paleointensities (Fig. 3) are in the range expected for core dynamos in early planetesimals (12) and other large bodies. Hf/W chronometry indicates that metallic cores formed in planetesimals prior to the final assembly of chondrite parent bodies (33). Recent paleomagnetic analyses of angrites (12) indicate that dynamos were likely generated in convecting metallic cores lasting for ≥11 Ma after solar system formation. Because such bodies melt from the inside out, some may preserve an unmelted, relic chondritic surface that could be magnetized during metasomatism in the presence of a core dynamo. A simple interpretation of Allende's paleomagnetic record is therefore that the CV parent planetesimal is such a partially differentiated object. Therefore, despite widespread practice (e.g., ref. 26), the LT and MT magnetization in Allende cannot be used to constrain the intensity of early protoplanetary disk fields. The HT magnetization might be a preaccretional record of such fields as suggested by ref. 26, but more analyses are required to verify this possibility (see *SI Appendix*).

Planetesimals apparently evolved into a diversity of differentiated end states, from unmelted primitive bodies, to partially molten objects with primitive crusts, to fully melted objects. There should perhaps be extant samples derived from the once-hot interior of the CV parent body: Although oxygen isotope and other geochemical data clearly rule out the hypothesis of a single parent body for all meteorites, they permit the possibility that

some chondrite and some achondrite groups originated on a single body. In fact, such samples may already have been discovered. Perhaps metamorphosed CK chondrites (34), coarse-grained clasts in the CV chondrites Mokoia (2) and Y-86009 (35), and/or the metamorphosed chondrite NWA 3133 (36) are samples of the deep crust, whereas the Eagle Station pallasite grouplet (36) and the iron meteorites Bocaiuva and NWA 176 (36) are samples from the melted interior. Further geochemical analyses of these meteorites are required to validate this hypothesis.

Our results suggest that asteroids with differentiated interiors could be present today but masked under chondritic surfaces, which would explain the great discrepancy between the >80% of meteorite parent bodies that melted versus the paucity of asteroids with basaltic surfaces (37). In fact, CV chondrites have spectral signatures similar to many members of the Eos dynamical asteroid family; the spectral diversity of this family has already led to suggestion that the parent asteroid was partially differentiated (38). In any case, the very existence of primitive achondrites, which contain evidence of relict chondrules, metamorphism, and partial melting, are *prima facie* evidence for the past existence of partially differentiated bodies.

**ACKNOWLEDGMENTS.** We thank J. Boesenberg and the American Museum of Natural History for providing sample of Allende; L. C. Alexander, S. Bowring, N. Dauphas, M. Funaki, R. Hewins, A. Irving, S. Jacobsen, A. Jambon, E. Lima, D. Mittlefehldt, B. Zanda, Y. Gallet, and M. Zuber for discussions; M. Boustie and L. Berthe for assisting with the laser shock experiments; J. Kirschvink for sharing automated sample handling technology; and K. Willis and B. Carbone for administrative help. B.P.W. thanks the Victor P. Starr Career Development Professorship and the National Aeronautics and Space Administration Origins of Solar Systems Program, and D.L.S. thanks the Ann and Gordon Getty Foundation fund for support.

- Wood JA (1988) Chondritic meteorites and the solar nebula. *Annu Rev Earth Planet Sci* 16:53–72.
- Krot AN, et al. (2006) *Meteorites and the Early Solar System II*, eds DS Lauretta and HY McSween (University of Arizona Press, Tucson, AZ), pp 525–553.
- Scott ERD, Keil K, Stöffler D (1992) Shock metamorphism of carbonaceous chondrites. *Geochim Cosmochim Acta* 56:4281–4293.
- Nagata T, Funaki M (1983) Paleointensity of the Allende carbonaceous chondrite. *Mem Natl Inst Polar Res Spec Issue* 30:403–434.
- Wasilewski P (1981) New magnetic results from Allende C3(V). *Phys Earth Planet Inter* 26:134–148.
- Acton G, et al. (2007) Micromagnetic coercivity distributions and interactions in chondrules with implications for paleointensities of the early solar system. *J Geophys Res* 112, 10.1029/2006JB004655.
- Flores-Gutiérrez D, Fucugauchi JU (2002) Hysteresis properties of chondritic meteorites: New results for chondrules from the Allende meteorite. *Geofis Int* 41:179–188.
- Thorpe AN, Senftle FE, Grant JR (2002) Magnetic study of magnetite in the Tagish Lake meteorite. *Meteorit Planet Sci* 37:763–771.
- Butler RF (1972) Natural remanent magnetization and thermomagnetic properties of Allende meteorite. *Earth Planet Sci Lett* 17:120–128.
- Sugiura N, Strangway DW (1985) NRM directions around a centimeter-sized dark inclusion in Allende. *Proceedings of the Fifteenth Lunar and Planetary Science Conference* (American Geophysical Union, Washington, DC), pp C729–C738.
- Wasilewski PJ, Saralark C (1981) Stable NRM and mineralogy in Allende: Chondrules. *Proceedings of the Twelfth Lunar and Planetary Science Conference* (Pergamon, New York), pp 1217–1227.
- Weiss BP, et al. (2008) Magnetism on the angrite parent body and the early differentiation of planetesimals. *Science* 322:713–716.
- Connelly JN, Amelin Y, Krot AN, Bizzarro M (2008) Chronology of the solar system's oldest solids. *Astrophys J* 675:L121–L124.
- Bizzarro M, Baker JA, Haack H (2004) Mg isotope evidence for contemporaneous formation of chondrules and refractory inclusions. *Nature* 431:275–278.
- Jogo K, Nakamura T, Ito M, Messenger S (2010) Mn–Cr systematics of secondary fayalites in the CV3 carbonaceous chondrites A881317, MET00430 and MET01074. *Lunar Planet Sci* 41:1573.
- Brearely AJ (1997) Disordered biopyroxenes, amphibole, and talc in the Allende meteorite: Products of nebular or parent body aqueous alteration? *Science* 276:1103–1105.
- Zaikowski A (1980) I–Xe dating of Allende inclusions: Antiquity and fine structure. *Earth Planet Sci Lett* 47:211–222.
- Hohenberg CM, Pravdivtseva OV, Meshik AP (2004) Trapped Xe and I–Xe ages in aqueously altered CV3 meteorites. *Geochim Cosmochim Acta* 68:4745–4763.
- Blum JD, Wasserburg GJ, Hutcheon ID, Stolper EM (1989) Origin of opaque assemblages in C3V meteorites: Implications for nebular and planetary processes. *Geochim Cosmochim Acta* 53:543–556.
- Urey HC (1956) Diamonds, meteorites, and the origin of the solar system. *Astrophys J* 124:623–637.
- Urey HC (1959) Primary and secondary objects. *J Geophys Res* 64:1721–1737.
- Clayton RN, Mayeda TK (1996) Oxygen isotope studies of achondrites. *Geochim Cosmochim Acta* 60:1999–2017.
- Trieloff M, et al. (2003) Structure and thermal history of the H-chondrite parent asteroid revealed by thermochronometry. *Nature* 422:502–506.
- Funaki M (2005) Natural remanent magnetization of chondrites and the magnetic field of protoplanets. *J Magn Soc Jpn* 29:918–925.
- Nagata T (1979) Meteorite magnetism and the early solar system magnetic field. *Phys Earth Planet Inter* 20:324–341.
- Sugiura N, Strangway DW (1988) *Meteorites and the Early Solar System*, eds JF Kerridge and MS Mathews (University of Arizona Press, Tucson, AZ), pp 595–615.
- Hood LL, Cisowski CS (1983) Paleomagnetism of the Moon and meteorites. *Rev Geophys Space Phys* 21:676–684.
- Banerjee SK, Hargraves RB (1972) Natural remanent magnetizations of carbonaceous chondrites and magnetic fields in early solar system. *Earth Planet Sci Lett* 17:110–119.
- Sugiura N, Lanoix M, Strangway DW (1979) Magnetic fields of the solar nebula as recorded in chondrules from the Allende meteorite. *Phys Earth Planet Inter* 20:342–349.
- Russell SS, et al. (2006) *Meteorites and the Early Solar System II*, eds DS Lauretta and HY McSween (University of Arizona Press, Tucson, AZ), pp 233–251.
- Hood LL, Artemieva NA (2008) Antipodal effects of lunar basin-forming impacts: Initial 3D simulations and comparisons with observations. *Icarus* 193:485–502.
- Wilson L, et al. (1999) Early aqueous alteration, explosive disruption, and reprocessing of asteroids. *Meteorit Planet Sci* 34:541–557.
- Kleine T, et al. (2005) Early core formation in asteroids and late accretion of chondrite parent bodies: Evidence from <sup>182</sup>Hf–<sup>182</sup>W in CAIs, metal-rich chondrites, and iron meteorites. *Geochim Cosmochim Acta* 69:5805–5818.
- Greenwood RC, Franchi IA, Kearsley AT, Alard O (2010) The relationship between CK and CV chondrites. *Geochim Cosmochim Acta* 74:1684–1705.
- Jogo K, Nakamura T (2009) A metamorphosed olivine-rich aggregate in the CV3 carbonaceous chondrite Y-86009. *72nd Annual Meteoritical Society Meeting* (Meteoritical Society, Tucson, AZ) p 5188.
- Irving AJ, et al. (2004) A primitive achondrite with oxygen isotopic affinities to CV chondrites: Implications for differentiation and size of the CV parent body. *Eos Trans Am Geophys Union* 85(Suppl):P31C-02.
- Meibom A, Clark BE (1999) Evidence for the insignificance of ordinary chondritic material in the asteroid belt. *Meteorit Planet Sci* 34:7–24.
- Mothe-Diniz T, Carvano JM, Bus SJ, Burbine TH (2008) Mineralogical analysis of the Eos family from near-infrared spectra. *Icarus* 195:277–294.

## Supporting Information Appendix

Magnetic Evidence for a Partially Differentiated Carbonaceous Chondrite Parent Body

*Proc. Natl. Acad. Sci. USA*

L. Carporzen, B.P. Weiss, L. Elkins-Tanton, D.L. Shuster, D.S. Ebel, and J. Gattacceca

**1. Natural remanent magnetization (NRM):** We extracted 71 bulk (matrix  $\pm$  chondrules  $\pm$  refractory inclusions) subsamples from AMNH5056 (Fig. S1a) using nonmagnetic tools and a precision wafering saw. These subsamples, ranging in volume from  $\sim 2$  to  $\sim 900 \text{ mm}^3$ , were then attached to nonmagnetic quartz disks using either cyanoacrylate cement or sodium silicate. We photographed all samples prior to subsectioning in order to maintain their mutual orientation. We estimate the orientation uncertainty of the subsamples to be  $\sim 5\text{--}10^\circ$ . All NRM measurements and most rock magnetic measurements were made in the MIT Paleomagnetism Laboratory.

**Alternating field (AF) demagnetization.** AF demagnetization and related rock magnetic remanence experiments were conducted on samples from AMNH5056 using an automated sample handling system integrated with the magnetometer (39). Twenty eight interior samples and thirteen exterior samples were subjected to three axis (up to 85 mT) followed by single axis (85 to 290 mT) AF demagnetization (main text Fig. 1). Four more interior samples were subjected to three axes AF demagnetization in each of the three orthogonal axes up to 290 mT to test for the possible deflection of the NRM direction due to single axis AF demagnetization, spurious gyromagnetic remnant magnetization and/or field-impressed anisotropy (40–45). For these samples, the magnetization vector at each AF step was computed using the Zijderveld-Dunlop averaging method (45). For each three axis AF step, all three uniaxial AF measurements for the latter four samples had nearly identical directions (within  $10^\circ$ ) and intensities ( $<1\%$  variation) (Fig. 1a and b). This indicates that unlike some other extraterrestrial samples (46), Allende is not very susceptible to GRM-acquisition. However, there was a slight decrease in the rate of demagnetization above 85 mT during single axis demagnetization compared to three axis demagnetization. AF demagnetization up to 290 mT was usually incapable of achieving complete removal of the NRM.

**Thermal demagnetization.** We conducted thermal demagnetization in an ASC Scientific oven (dc field  $<20 \text{ nT}$ ) in air with heating times ranging from 45 to 75 minutes (see Table S1, Figs. S2–4, and main text Figs. 1–2). Because the sodium silicate used to hold

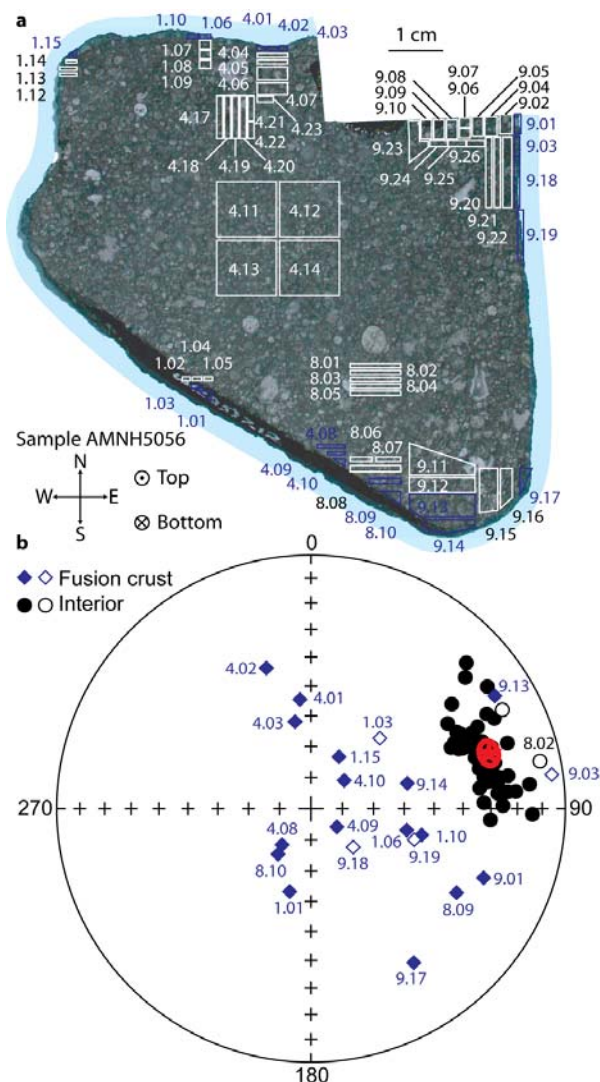


**Fig. S1.** **a**, Photograph of Allende sample AMNH5056 showing our sampling locations (polygons) and corresponding subsample numbers. This was from a stone collected by G. Wasserburg from the Allende fall site in 1969. The sides of the slab shaded light blue are covered with fusion crust from atmospheric passage. Blue polygons = fusion-crusted subsamples; white polygons = interior subsamples. All subsamples are mutually oriented and referenced to the arbitrary coordinate system described by the compass at lower left. **b**, Equal area plot showing directions of NRM of subsamples from the interior (black dots) and fusion-crusted exterior (blue diamonds). Solid symbols = lower hemisphere; open symbols = upper hemisphere. Equal area plot is oriented in the same way as slab in **a**, with inclination =  $90^\circ$  oriented out of the page (perpendicular to the slab saw cut plane) and declination =  $0^\circ$  oriented toward top of the page. Red star = average direction of the 51 interior subsamples assuming a Fisher distribution (95% confidence interval given by red ellipsoid). This direction is statistically different than the directions of fusion crust samples, which constitutes

a fusion-crust baked contact test that the NRM in Allende is preterrestrial.

the samples on the quartz disks becomes brittle during thermal demagnetization, each sample was reoriented using photographs following heating and prior to remanence measurements. By the end of these thermal demagnetization experiments, some samples acquired a reddish colouration, indicating that they were probably partly altered by this process.

We thermally demagnetized 19 interior and 7 exterior samples (Table S1, Figs. 1, 2 and S3). For 7 selected samples (9.11, 9.12, 9.13, 9.14, 9.15, 9.16, and 9.17), a total of 35 thermal demagnetization steps (NRM, 50°C, 100 to 190°C at 30°C intervals, 210 to 290°C at 20°C intervals, 300 to 400°C at 10°C intervals, and 420 to 660°C at 20°C intervals) were performed (Fig. S3i-l and t). A second set of 7 samples (4.10, 9.03, 9.18, 9.19, 9.20, 9.21, and 9.22) was subjected to a total of 20 thermal demagnetization steps (NRM, 50°C, 100 to 190°C at 30°C intervals, 210 to 310°C at 20°C intervals, 340 to 380°C at 20°C intervals, and 420 to 580°C at intervals of 40°C) were performed (Fig. S3m-o and t). A set of 4 additional samples (9.23, 9.24, 9.25, and 9.26) was subjected to a total of 14 thermal demagnetization steps with higher temperature resolution near the upper blocking temperature limit of the middle temperature (MT) component (NRM, 100 to 200°C at 50°C intervals, 230°C, 250°C, 270°C, 280 to 300°C at 5°C intervals, 310°C, and 320°C) (Fig. S3p-s). Finally, a set of 4 samples (4.11, 4.12, 4.13, and 4.14) was subjected to 11 thermal demagnetization steps (NRM, 100 to 250°C at 50°C intervals and 270 to 320°C at 10°C intervals) (Fig. S3a-d).

*NRM of fusion crusted samples.* Our exterior subsamples of AMNH5056 each consist of a thin (<1 mm thick) fusion crust attached to several mm or more of unmelted interior material. Because the fusion crust samples each also contain interior material that extends beyond the expected thermal remagnetization zone, they should contain a mixture of both fusion crust magnetization as well as unbaked interior magnetization. AF demagnetization did in fact reveal that fusion crusted samples have at least three components: scattered low coercivity (LC) magnetization blocked up to ~10 mT and two or more scattered high coercivity (HC) components blocked from ~10 to 290 mT (Table S1 and main text Figs. 1f and 2b). These components are oriented differently than the LC and HC components in interior samples. We did not conduct least squares fits to these components because they are a

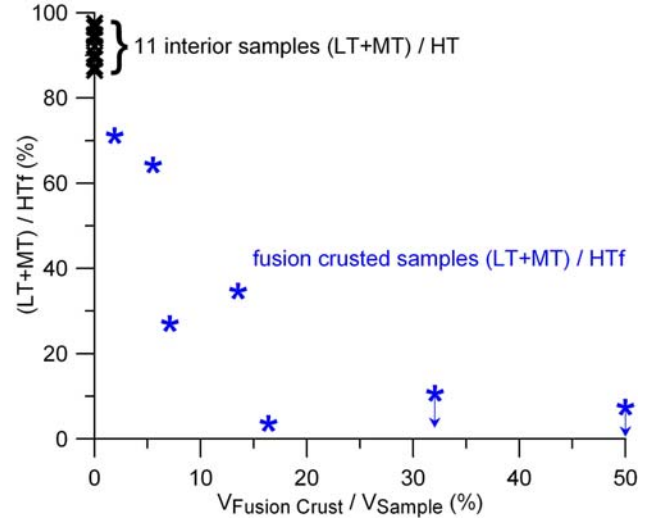


**Fig. S2.** Relationship between volume fraction of fusion crust and relative amount of HTf magnetization in exterior samples. Plotted as blue stars is the ratio of the sum of the LT and MT components to the HTf component,  $(LT+MT)/HTf$ , versus the ratio of the fusion crust volume to the total volume of each sample,  $V_{\text{fusion crust}}/V_{\text{sample}}$ . Interior samples (which contain no fusion crust) are plotted as black crosses for comparison at  $V_{\text{fusion crust}}/V_{\text{sample}} = 0\%$ . For the latter samples, which contain HT rather than HTf magnetization, the ordinate is defined as the ratio of the sum of the LT and MT components to the HT magnetization. Errors in volume estimates could be as high as 5-10%. This figure shows that the NRM of the two samples with the largest volume fraction of fusion crust (at right) contain <10% contributions from LT + MT components and have orientations statistically different from the interior samples.

complex mixture of interior and exterior magnetization components that are not isolated with AF methods. Our thermal demagnetization of the fusion crusted samples isolated unidirectional low temperature (LT) and MT components (oriented similarly to those of interior samples) and scattered high temperature magnetization directions (HTf) (Fig. 2). A major contributor to the latter magnetization must be magnetite formed in the fusion crust during atmospheric passage. Therefore, we label it HTf (for high temperature fusion crust component) to distinguish it genetically from the scattered high temperature (HT) directions of the interior samples. Because of the large amount of magnetized magnetite, the HTf magnetization is stable to much higher temperatures and much stronger in intensity than the HT magnetization in interior samples.

This might at first seem suggest that the LT and MT components in both sample types are predominantly a terrestrial overprint. However, as discussed above, most of our fusion crusted subsamples are actually composed of substantial amounts (80-90

Label	Dec (°)	Inc (°)	N	MAD / $\alpha_{95}$ (°)	k / Mass (g)	Remarks
<b>Interior subsamples</b>						
<b>NRM</b>	<b>72.7</b>	<b>27.6</b>	<b>51</b>	<b>3.4</b>	<b>34.5</b>	
1.02	46.2	23.2	81	7.5	-	10-290 mT
1.04	45.9	21.7	81	5.5	-	10-290 mT
1.05	53.7	28.0	81	6.0	-	10-290 mT
1.07	77.2	30.9	81	7.1	-	10-290 mT
1.08	80.2	38.4	81	12.3	-	10-290 mT
1.09	77.9	23.0	81	5.7	-	10-290 mT
1.12	61.0	32.3	81	5.1	-	10-290 mT
1.13	58.5	17.0	81	4.6	-	10-290 mT
1.14	52.9	33.5	81	12.5	-	10-290 mT
4.04	66.6	35.9	81	3.4	0.0668	10-290 mT
4.05	76.8	38.7	81	5.5	0.07	10-290 mT
4.06	66.7	41.7	81	9.9	0.224	10-290 mT
4.07	71.7	33.8	81	3.1	0.1956	10-290 mT
4.21	72.8	30.7	81	4.0	0.1237	10-290 mT
4.22	73.4	30.0	81	5.1	0.0423	10-290 mT
4.23	74.9	34.0	81	3.1	0.0769	10-290 mT
8.01	66.6	29.9	81	4.0	0.007	10-290 mT
8.02	60.8	29.0	81	35.3	0.053	10-290 mT
8.03	77.0	21.0	81	18.5	0.157	10-290 mT
8.04	71.8	29.3	81	4.2	0.061	10-290 mT
8.05	68.8	23.1	81	5.0	0.011	10-290 mT
8.06	64.4	23.9	81	4.2	0.042	10-290 mT
8.07	61.9	10.9	81	14.5	0.019	10-290 mT
8.08	50.1	13.9	81	2.9	-	10-290 mT
9.02	79.9	37.4	81	6.0	0.0557	10-290 mT
9.04	65.9	32.8	81	4.6	0.1111	10-290 mT
9.05	75.3	31.8	120	11.4	0.2118	10-290 mT
9.06	66.8	32.6	81	5.3	0.097	10-290 mT
9.07	71.2	36.5	81	5.4	0.0326	10-290 mT
9.08	92.4	33.7	81	5.0	0.1867	10-290 mT
9.09	80.8	37.3	81	3.6	0.1288	10-290 mT
9.10	88.6	37.3	81	9.0	0.1822	10-290 mT
<b>HC</b>	<b>68.3</b>	<b>30.3</b>	<b>32</b>	<b>3.9</b>	<b>43.4</b>	
4.11LT	81.7	30.9	4	2.6	2.8017	NRM-200°C
4.12LT	81.1	28.5	4	3.8	2.5865	NRM-200°C
4.13LT	78.7	30.0	4	1.9	2.8129	NRM-200°C
4.14LT	80.8	29.5	4	2.5	2.8126	NRM-200°C
4.17LT	86.0	37.6	4	2.7	0.6032	NRM-200°C
4.18LT	84.5	35.2	4	2.6	0.5145	NRM-200°C
4.19LT	84.6	34.8	4	3.5	0.3675	NRM-200°C
4.20LT	83.0	36.6	4	1.9	0.2880	NRM-200°C
9.11LT	76.4	36.4	6	4.5	0.7516	NRM-190°C
9.12LT	72.1	36.4	6	1.9	0.5712	NRM-190°C
9.15LT	66.0	37.1	6	4.6	0.4272	NRM-190°C
9.16LT	72.2	37.2	6	2.3	0.2642	NRM-190°C
9.20LT*	71.9	-18.2	6	5.5	0.4279	NRM-190°C
9.21LT	73.2	37.6	6	3.1	0.3112	NRM-190°C
9.22LT	73.6	35.7	6	1.2	0.6143	NRM-190°C

Label	Dec (°)	Inc (°)	N	MAD / $\alpha_{95}$ (°)	k / Mass (g)	Remarks
9.23LT	70.9	31.2	4	2.1	0.6827	NRM-200°C
9.24LT	82.4	32.3	4	3.1	0.1686	NRM-200°C
9.25LT	88.5	30.7	4	4.4	0.0804	NRM-200°C
9.26LT	85.6	31.1	4	4.6	0.062	NRM-200°C
<b>LT</b>	<b>79.0</b>	<b>34.0</b>	<b>18</b>	<b>2.6</b>	<b>174.5</b>	
4.11MT	64.5	22.4	5	1.2	2.8017	200-290°C
4.12MT	68.0	25.5	5	0.7	2.5865	200-290°C
4.13MT	64.9	25.4	5	1.0	2.8129	200-290°C
4.14MT	67.9	25.0	5	1.0	2.8126	200-290°C
4.17MT	68.9	32.1	7	4.3	0.6032	200-290°C
4.18MT	69.1	27.4	7	3.7	0.5145	200-290°C
4.19MT	66.7	28.3	7	4.4	0.3675	200-290°C
4.20MT	65.5	28.8	7	3.7	0.2880	200-290°C
9.11MT	57.4	32.4	5	3.7	0.7516	210-290°C
9.12MT	50.5	28.7	5	1.2	0.5712	210-290°C
9.15MT	57.3	33.1	5	2.3	0.4272	210-290°C
9.16MT	53.0	29.8	5	1.6	0.2642	210-290°C
9.20MT*	47.4	-15.2	5	1.9	0.4279	210-290°C
9.21MT	51.2	35.1	5	2.8	0.3112	210-290°C
9.22MT	59.5	31.8	5	2.0	0.6143	210-290°C
9.23MT	57.7	26.4	7	1.5	0.6827	200-290°C
9.24MT	63.1	28.8	7	3.6	0.1686	200-290°C
9.25MT	75.7	28.7	7	5.0	0.0804	200-290°C
9.26MT	69.8	28.3	7	7.1	0.062	200-290°C
<b>MT</b>	<b>62.9</b>	<b>29.0</b>	<b>18</b>	<b>3.0</b>	<b>135.6</b>	
9.11HT	40.4	57.2	13	19.5	0.7516	300-440°C
9.12HT	359.8	41.0	13	9.8	0.5712	300-440°C
9.15HT	1.8	62.5	5	5.3	0.4272	290-330°C
9.16HT	356.9	45.2	9	8.8	0.2642	290-370°C
9.20HT	29.3	47.6	9	35.0	0.4279	310-580°C
9.21HT	20.1	65.2	5	9.2	0.3112	290-380°C
9.22HT	71.6	-11.3	4	4.5	0.6143	290-360°C
<b>Fusion crusted subsamples</b>						
1.01	358.5	-49.3	61	33.4	-	25-290 mT
1.03	352.5	-67.2	81	5.9	-	10-290 mT
1.06	98.2	62.6	81	5.6	-	10-290 mT
1.10	95.1	63.5	81	5.2	-	10-290 mT
1.15	337.4	-37.3	46	11.9	-	40-290 mT
4.01	334.9	64.4	91	9.5	0.009	5-290 mT
4.02	310.0	34.3	91	10.7	0.017	5-290 mT
4.03	304.2	44.1	91	11.7	0.021	5-290 mT
4.08	306.7	-36.6	71	16.7	0.17355	15-290 mT
4.09	322.8	-56.6	71	14.2	0.0074	15-290 mT
8.09	30.3	-16.8	71	19.6	0.02	15-290 mT
8.10	37.7	-53.4	61	19.1	0.063	25-290 mT
9.01	342.1	46.0	66	13.9	0.0323	20-290 mT
4.10LT	56.1	65.6	6	9.5	0.1539	NRM-190°C
9.03LT	70.4	33.8	6	3.6	0.1977	NRM-190°C
9.13LT	68.2	34.3	6	3.2	0.5853	NRM-190°C
9.14LT	66.0	26.7	6	16.1	0.2089	NRM-190°C



Label	Dec (°)	Inc (°)	N	MAD / $\alpha_{95}$ (°)	k / Mass (g)	Remarks
9.17LT	62.5	17.1	6	6.0	0.1015	NRM-190°C
9.18LT	80.5	-12.6	6	18.8	-	NRM-190°C
9.19LT	94.0	20.4	6	10.6	-	NRM-190°C
<b>LT</b>	<b>72.5</b>	<b>26.9</b>	<b>7</b>	<b>19.8</b>	<b>10.2</b>	
4.10MT	63.9	66.8	5	6.8	0.1539	210-290°C
9.03MT	55.9	19.6	5	3.5	0.1977	210-290°C
9.13MT	52.8	24.8	5	1.6	0.5853	210-290°C
9.14MT	54.0	-0.7	5	31.8	0.2089	210-290°C
9.17MT	72.9	8.6	5	20.2	0.1015	210-290°C
9.18MT	182.2	-14.7	5	31.0	-	210-290°C
9.19MT	80.0	-71.5	5	23.2	-	210-290°C
<b>MT</b>	<b>47.7</b>	<b>33.7</b>	<b>7</b>	<b>35.7</b>	<b>3.8</b>	
4.10HTf	154.7	56.2	4	13.8	0.1539	380-500°C
9.03HTf	164.2	-18.2	4	8.7	0.1977	380-500°C
9.13HTf	174.9	-41.7	6	35.3	0.5853	400-500°C
9.14HTf	91.7	74.1	6	3.7	0.2089	400-500°C
9.17HTf	173.4	17.6	6	5.7	0.1015	400-500°C
9.18HTf	178.5	-21.2	4	11.4	-	400-500°C
9.19HTf	164.8	-0.7	3	5.4	-	400-460°C

**Table S1.** Fisher statistical analysis (47) and principal component analyses (48) for both AF and thermal demagnetization. The first column gives the average name (bold) or subsample number from AMNH5056, the second column gives the mean component (or subsample) declination, the third column gives the mean component (or subsample) inclination, the fourth column gives the number of average directions (or demagnetization steps), the fifth column gives the 95% confidence interval (or maximum angular deviation MAD), the sixth column gives the precision parameter (or subsample mass (in g) when measured during extraction), and the seventh column gives the alternating field or temperature range used during principal component analysis. Note that although AF demagnetization did not isolate a distinct LT-like direction, the scatter in the HC directions encompasses that of the LT and MT components and the mean HC direction lies between that of the LT and MT components (Fig. 2a). This indicates that the LT and MT components have overlapping coercivity spectra and both contribute to the HC component (4).

volume %) of interior material. Therefore, an alternative possibility is that the LT + MT components in fusion crusted samples are simply a manifestation of remanence blocked in the unbaked interior fraction of the samples that was demagnetized at low temperatures (with the fusion crust portion containing little remanence blocked at these temperatures). These two possibilities can be distinguished by comparing the relative intensity of the LT + MT components to the HTf component with the volume ratio of fusion crust to interior material in each sample. By visual inspection, we estimated the fusion crust thickness to be  $\leq 1$  mm.

The first (terrestrial overprint) hypothesis would predict that the ratio of the LT + MT components to

the HTf component should be independent of the ratio of fusion crust to interior material, while the second hypothesis would predict that these should be negatively correlated. In fact, we clearly observe the latter: the greater the relative fraction of fusion crust, the less the LT and MT components contribute to the HTf component and to the total NRM (Fig. S2). In particular, the NRMs of the two samples with the largest volume fraction of fusion crust (9.18 and 9.19) contain  $<10\%$  contributions from LT + MT components and have orientations statistically different from the interior samples.

This demonstrates that the MT and LT components are carried only by the unmelted interior of each subsample. That is, the LT and MT components in exterior samples are *not* primarily from baking during atmospheric passage. Instead, it is the HTf magnetization that is predominantly from atmospheric passage (although the unbaked interior of the fusion crusted samples likely contributes a small amount of HT magnetization to this component). The orientation of the MT magnetization of pure interior samples is different from the individual HTf directions of the exterior samples to  $>95\%$  confidence (Fig. 2, Table S1), as observed previously (4, 9, 10).

The exterior side of sample 9.22 is located  $\sim 1$  mm below the East fusion crust and yet the sample shows no evidence of thermal remagnetization from atmospheric passage. This indicates that the baked zone from the fusion crust should not exceed  $\sim 1$  mm deep for Allende, similar to that observed in other stony meteorites. This constitutes a positive baked contact test demonstrating that the majority of the interior magnetization is preterrestrial.

**2. Origin of the interior NRM:** To precisely determine the upper blocking temperature limit of Allende's MT component, we conducted high resolution thermal demagnetization of its NRM and a laboratory partial thermoremanent magnetization (pTRM) acquired during cooling from 320°C (chosen because it is the Curie temperature of pyrrhotite) in a 16  $\mu$ T field for eight interior samples. Four of these samples were later given a shock remanent magnetization (SRM) in either a 500  $\mu$ T field (three samples) or 800  $\mu$ T (one sample) by  $\sim 3 \pm 0.5$  GPa laser shock (49) and were then again thermally demagnetized. The peak-shock temperature increase during these experiments was negligible (49, 50). Another never-before thermally demagnetized sample was given a laboratory 0.9 T saturation [reached



at 0.6 T (6)] isothermal remanent magnetization (IRM), thermally demagnetized, and then the experiment repeated.

*Comparison of NRM with pTRM, IRM, and SRM.* Changes in NRM directions (Fig. S3) and NRM intensities (Fig. S4) during thermal demagnetization precisely determine the upper limit of the MT component to be  $\sim 290 \pm 5^\circ\text{C}$ . This temperature is distinctly lower than the  $310\text{--}325^\circ\text{C}$  Curie point of pyrrhotite. The MT component also unblocks  $>25^\circ\text{C}$  below that of the  $320^\circ\text{C}$  laboratory pTRM (Fig. S4a-h) and unblocks much more rapidly than the IRM (Fig. S4i) and the SRM (Fig. S4a-d). This strongly suggests that the MT component is neither a  $320^\circ\text{C}$  pTRM, a crystallization remanent magnetization (CRM) from low-temperature formation of pyrrhotite<sup>a</sup>, an IRM, nor a SRM.

A second argument against an SRM origin for the MT component is that, given the linear relationship between SRM and field intensity [see (49) and also verified for Allende by a comparison of our SRM experiments in the 500 and 800  $\mu\text{T}$  fields], our experiments indicate that an extremely strong (600–700  $\mu\text{T}$ ) background field would be required to have produced the MT component by a 3–5 GPa shock. This argues against the presence of SRM from an impact event above the 2.8 GPa pyrrhotite phase-transformation pressure (51) as well as SRM from lower pressure shocks (which would require even stronger ambient fields to produce magnetization with intensity matching that of the NRM). Finally, the lack of MT magnetization above  $290^\circ\text{C}$  also rules out an accretional remanent magnetization acquired during parent body accretion in a magnetic field, which would otherwise have blocked NRM up to the meteorite's maximum Curie point of  $\sim 610^\circ\text{C}$  (4).

Fig. S4 shows that between  $\sim 220$  and  $290^\circ\text{C}$ , which is nearly the entire temperature range of the MT component as indicated by directional data (Fig. 1), the NRM unblocks at similar rate as the laboratory pTRM. This strongly supports a pTRM origin for the MT component. On the other hand, the LT component, which spans the temperatures below  $\sim 200^\circ\text{C}$ , clearly unblocks more rapidly than the pTRM. This provides strong indication that the LT component is not thermoremanent in origin. In

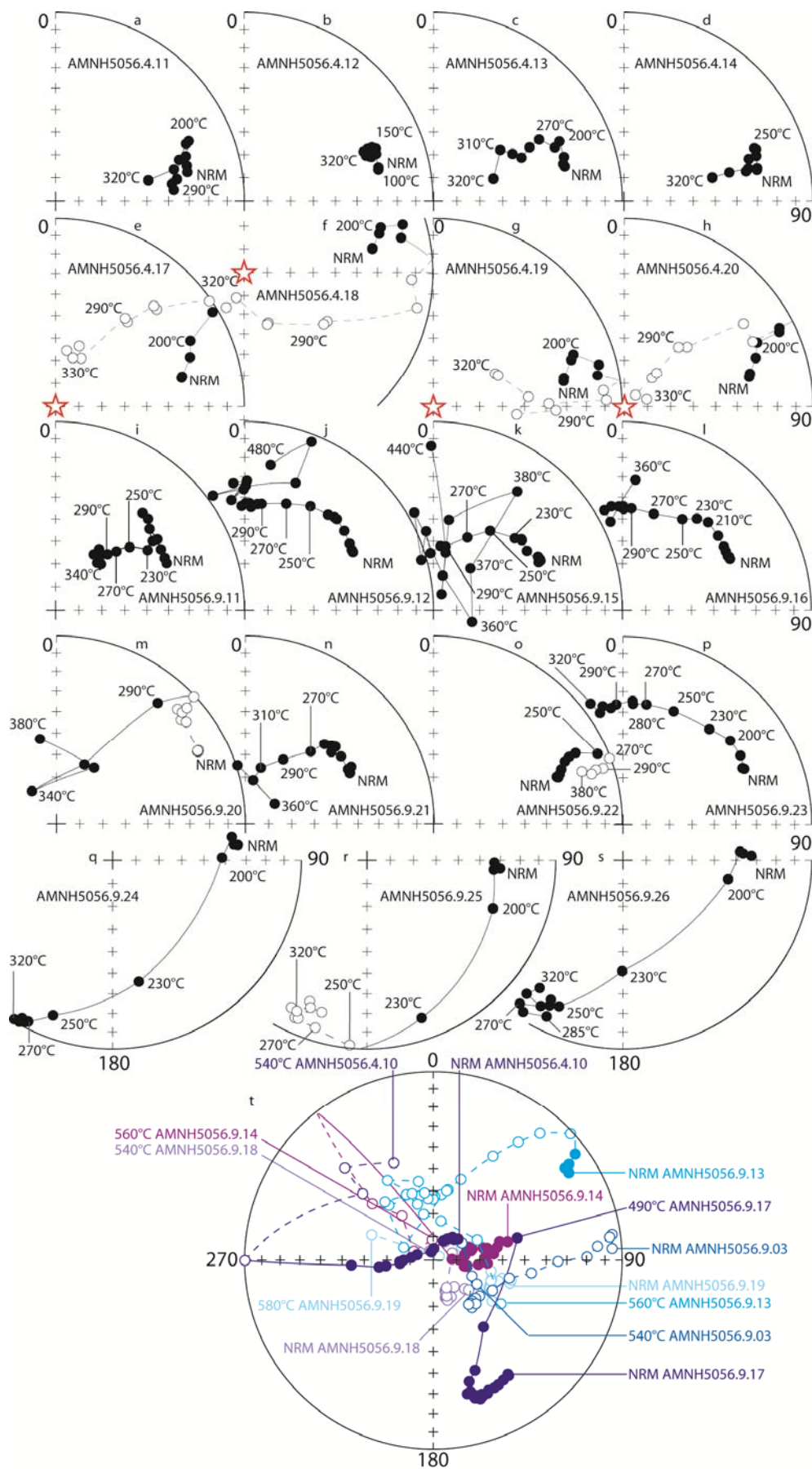
fact, as described in Section 4 below, there is good reason to believe the LT component is a long-term VRM acquired from fine-scale magnetostatic interactions on the parent body over the last 4.5 Ga.

*Notes on sample alteration.* Another possible indication for a shock origin of the MT component could be that the NRM is carried by metastably magnetized hexagonal pyrrhotite rather than stable monoclinic pyrrhotite (52). The former can be recognized by (a) significant unblocking of IRM at  $240\text{--}265^\circ\text{C}$  during a first thermal demagnetization sequence and less unblocking at this temperature during subsequent runs conducted following reacquisition of a new IRM (due to conversion from the metastable ferrimagnetic to stable antiferromagnetic form), and (b) a reduced overall moment and susceptibility at all blocking temperatures below  $240\text{--}265^\circ\text{C}$  [due to the permanent destruction of the metastable ferrimagnetic phase] (53–57). Although we found that the sample did exhibit  $\sim 15\%$  less unblocking between 200 and  $265^\circ\text{C}$  during the second run relative to the first (Fig. S4i), this unblocking occurs at higher temperatures and to a much reduced extent relative to that for meteorites inferred to be dominated by metastable ferrimagnetic pyrrhotite (53). Furthermore, there were only subtle changes in susceptibility before and after thermal demagnetization of NRM and pTRM (Fig. S4a-d). Additionally, the IRM was actually stronger after demagnetization to temperatures  $>200^\circ\text{C}$  following heating (Fig. S4i), indicating that either magnetite was produced from oxidation of monoclinic pyrrhotite and metal and/or monoclinic pyrrhotite was produced from oxidation of hexagonal pyrrhotite (58). Finally, our low-temperature experiments (Fig. S8) identified a 34 K remanence transition indicative of monoclinic pyrrhotite.

The consequences of the above data are threefold. First, the main ferromagnetic sulfide is likely monoclinic pyrrhotite. Second, the observed differences between the NRM and pTRM unblocking spectra in Fig. S9 are likely partly due to sample alteration.

**Fig. S3. (following page)** Equal area plots showing directions of NRM during thermal demagnetization of Allende subsamples from sample AMNH5056.9. Interior subsamples (i-n, p) have clustered HT directions between  $400$  and  $500^\circ\text{C}$  whereas interior subsample 9.22 (o) has a magnetization closer to fusion crust subsamples 9.03 and 9.18. Interior subsamples (a-d, p-s) were demagnetized up to  $320^\circ\text{C}$ . Interior subsamples (e-h) were demagnetized up to  $330^\circ\text{C}$  during palaeointensity experiments (Red stars represent the direction of the laboratory field). Fusion crusted subsamples (shown together in p) possess multi-component magnetizations blocked up to  $580^\circ\text{C}$ .

<sup>a</sup> As discussed in the main text, the MT component is carried predominantly by pyrrhotite. That awaruite and magnetite are not significant NRM carriers might at first seem to suggest that the MT component is a CRM from low-temperature sulfidization. However, magnetite and awaruite in Allende have relatively little remanence-carrying capacity below  $320^\circ\text{C}$  (see Fig. 5c, d of ref. 11).



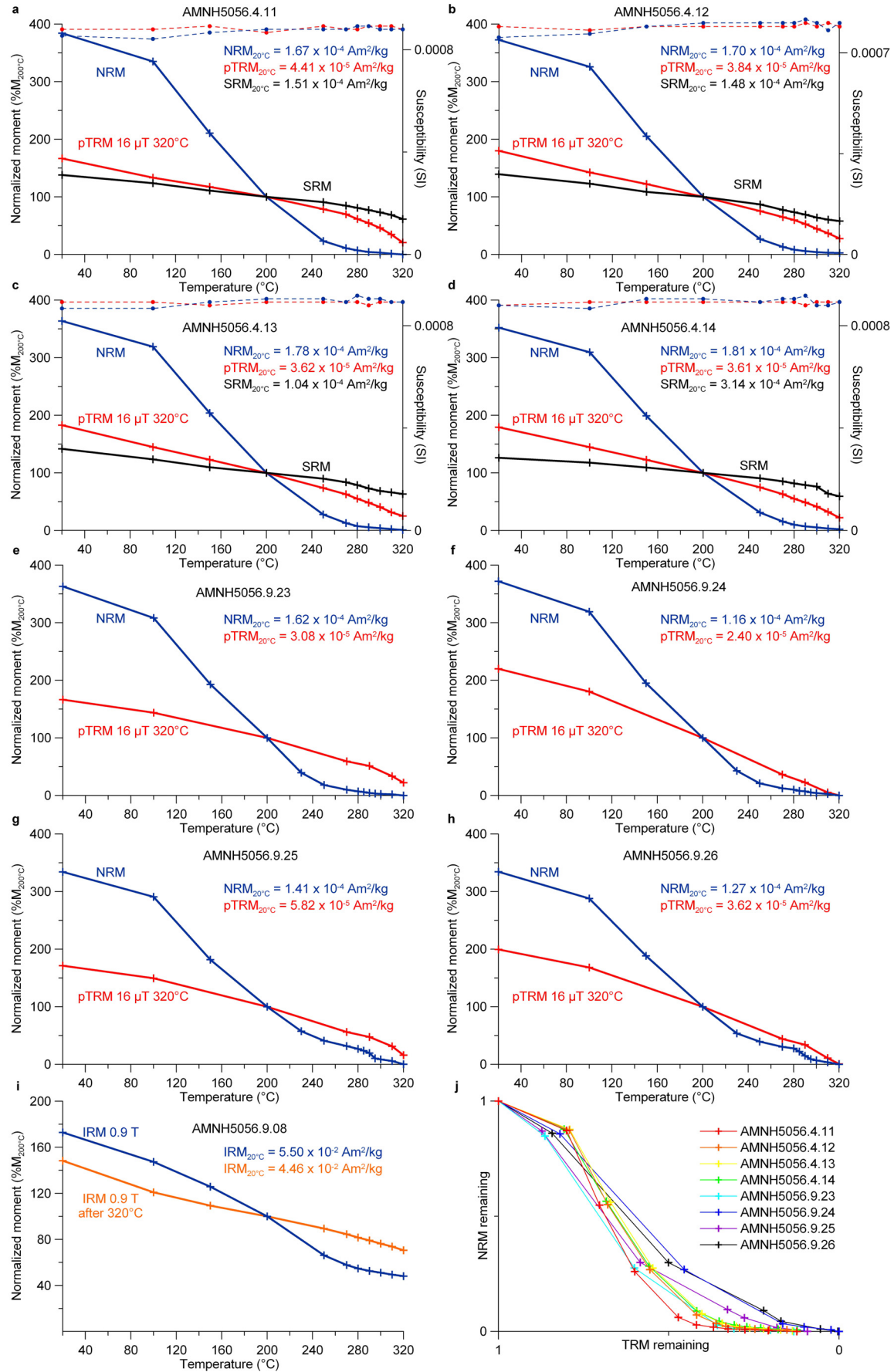


**Fig. S4. (previous page)** Thermal demagnetization of NRM (blue), laboratory pTRM (red), SRM (dark) and IRM for nine Allende subsamples from sample AMNH5056.9 (see Figs. S1a and S3a-d, l-o). The NRM intensity was computed using vector subtraction due its multicomponent nature. The laboratory pTRM (**a-h, j**) was acquired during cooling from 320°C in a field of 16  $\mu$ T after thermal demagnetization of the NRM up to 320°C. The susceptibility of the each sample (dashed curves in **a-d**) was observed to be approximately constant through the measurements. The SRM was acquired by laser shock in the presence of a (**a-c**) 500  $\mu$ T or (**d**) 800  $\mu$ T field. The uppermost 1-1.5 mm of the sample that suffered a peak shock pressure in the 2.5-3.5 GPa range was then subsectioned and used for these SRM thermal demagnetization measurements. As expected, the SRM was observed to have been acquired oriented in the same direction as that of the background field. After thermal demagnetization of IRM (blue curve in **i**), a second IRM was applied, followed by a second thermal demagnetization run (orange curve in **i**). All curves were normalized to their values at 200°C, the lower temperature limit of the MT component.

Third, sample alteration during thermal demagnetization limits our ability to strongly verify a thermoremanent origin for the MT component from the comparison of the rate of NRM unblocking above 200°C with the late of unblocking of a laboratory pTRM (see above).

Nevertheless, we conclude that there is overall strong evidence that the MT component is a pTRM or at least a thermochemical remanent magnetization (TCRM) acquired during cooling from metamorphic temperatures of 290°C in a magnetic field on the parent body. This could have been acquired either during metamorphism to a peak temperature of 290°C followed by cooling in a magnetic field, or else by metamorphism to a higher temperature followed by cooling in near-zero field until 290°C, at which point a field appeared and persisted for the remaining cooling [as first proposed by (4)]. If the peak metamorphic temperature of Allende were actually higher than 290°C, this would favor the latter scenario and also strengthen our interpretation that the magnetization in Allende is predominantly a post-accretional remanence acquired on the parent body.

*Origin of HT magnetization.* We have found a weak (several % of NRM) HT magnetization blocked above 290°C (Figs. 1c, d and S4) which is usually oriented in a direction distinct from that of the MT component, often does not reach origin-trending directions (Fig. 1c, d), and is highly non-unidirectional throughout the meteorite (Figs. 2 and S3). Similar results have been previously obtained

on Allende bulk samples and individual chondrules and have been ascribed to preaccretional remanence (10, 29). However, given the lack of stable, origin-trending HT magnetization, the fact that chondrules were spinning at high speeds when they cooled (59), evidence that Allende experienced pervasive parent body sulfidization and oxidation (see main text and Section 3), and the fact that our thermal demagnetization leads to sample alteration at high temperatures (see above), we believe that additional studies are required to establish the true nature of the HT magnetization. In particular, it is not yet clear whether the HT magnetization is even true a NRM component or rather an artifact of the demagnetization process.

**3. Petrologic thermal constraints:** The meteorite's low bulk-H<sub>2</sub>O content, the presence of talc and amphibole in chondrule phenocrysts (16), thermodynamic analysis of coexisting phases in opaque assemblages (19), olivine-spinel thermometry and Fe and Mg concentration gradients in olivine (60), the noble gas contents (61) and degree of graphitization (62) of nanodiamonds, the structure of organic matter (63), and oxygen isotope anomalies in alteration phases (64) collectively indicate that coincident with or following aqueous alteration, the meteorite was thermally metamorphosed to a peak temperature somewhere between ~250 and <600°C. The exact peak metamorphic temperature is uncertain due to the overall chemical disequilibrium in the meteorite and the possibility that the meteorite's constituents experienced heating in the nebula prior to accretion which would tend to decrease the peak metamorphic temperature [see nanodiamond data and organic thermometry that has been calibrated to the latter (63)]. The lower range of these temperatures is essentially indistinguishable from the 290°C peak blocking temperature of the MT component (Fig. S4).

*The ferromagnetic mineralogy of Allende.* Pyrrhotite, magnetite and awaruite have been reported to be the main ferromagnetic minerals in Allende (4, 6, 19, 65-73), with pyrrhotite as the main NRM carrier. The bulk composition of pyrrhotite in Allende (4, 19, 68, 74, 75) spans the range from monoclinic to hexagonal forms (76, 77). Our repeat thermal demagnetization of IRM experiment (Section 2), along with the low temperature data described in Section 4, suggest that the main ferromagnetic pyrrhotite phase is in the monoclinic rather than metastable hexagonal form.



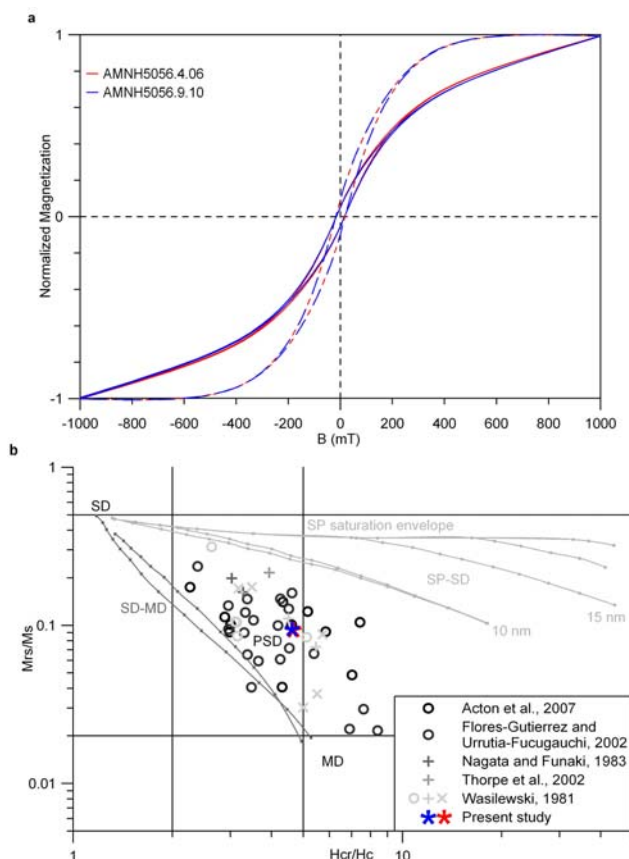


**Fig. S5.** **a**, Room temperature hysteresis loops on samples 4.06 (red) and 9.10 (blue). The high-field slope of each hysteresis loop was used to estimate the contribution of paramagnetic minerals. This contribution has been subtracted from the loops shown as dashed lines. **b**, Day plot (78, 79) of the ratio of coercivity of remanence to coercivity ( $H_{cr}/H_c$ ) versus the ratio of saturation remanence to saturation magnetization ( $M_{rs}/M_s$ ). Single domain (SD), pseudo single domain (PSD) and multidomain (MD) ranges calculated for magnetite are indicated, following ref. 79. Mixing lines between SD and MD and between SD and superparamagnetic (SP) of different sizes are also indicated, following ref. 79. Since Allende contains pyrrhotite and some metal in addition to magnetite, these lines are meant only as rough guidelines of magnetic domain state. Samples 4.06 (blue star) and 9.10 (open red star) are nearly indistinguishable. For comparison, also shown are previous hysteresis parameters obtained on Allende (4-8) for individual chondrules (circles), a matrix sample (cross), and bulk material (plus).

The chief magnetic evidence for these minerals is that numerous thermomagnetic curves (Fig. 5 of ref. 9, Fig. 6 of ref. 28, Fig. 1 of ref. 67, Figs. 4 and 8 of ref. 11, Figs. 2 and 3 of ref. 4) indicate major phases unblocking at 330°C (Curie point of pyrrhotite) and near 580-600°C (close to the Curie point of both magnetite and awaruite). These thermomagnetic data along with our low temperature magnetometry data (Section 4) indicate that magnetite ( $\pm$  awaruite) dominates the remanence-carrying capacity and rock magnetic properties of interior samples.

Early studies of Allende (4, 80) sometimes stated that the main  $\text{FeNi}_3$  phase in Allende is taenite ( $\gamma\text{-FeNi}_3$ ) rather than the isochemical mineral awaruite ( $\gamma'\text{-FeNi}_3$ ). Much of this confusion stems from the fact that the low-temperature portion of the Fe-Ni phase diagram was not well-understood until the late 1990s (see refs. 81, 82). In fact, transmission electron microscopy (71, 83) conclusively demonstrates that the dominant Ni-rich metal in Allende is awaruite. It has also been suggested that pentlandite is a remanence carrier in Allende (4, 72). Although pentlandite is indeed abundant in Allende (71), it is a Pauli paramagnetic mineral (52).

In addition to the major phases (pyrrhotite, magnetite and awaruite), Allende likely has several trace ferromagnetic phases. Microprobe analyses have identified kamacite (73, 84) as well as phosphorous-rich metal probably in the form of schreibersite (73). These analyses show that the vast majority of the metal in Allende is in the form of awaruite and that these are trace phases. This is supported by the fact that there is no evidence of their respective 780°C (55) and 420°C (85) Curie temperatures in thermal demagnetization of remanence or thermomagnetic data. Some Allende thermomagnetic curves (e.g., Fig. 1a,b of ref. 67, Fig. 8 and top left in Fig. 4 of ref. 11) also exhibit slight inflections at  $\sim 150^\circ\text{C}$ , although this is absent in many others (e.g., Figs. 2 and 3 of ref. 4, bottom left and right panels in Fig. 4 of ref. 11). This might be indicative of minor amounts of goethite in some samples, as also possibly indicated by some microprobe (73) and Mössbauer data (86, 87). However, other Mössbauer and Raman studies did not identify goethite (88-90). Our low temperature studies (see Section 4 Inverse TRM below) also show no evidence of hematite's Morin transition (e.g., 91). *In fact, we are aware of no unambiguous evidence for goethite, hematite, or any other terrestrial weathering ferromagnetic phases in Allende. This is as expected for a meteorite fall which was picked up almost immediately after landing on Earth. Therefore, even if Allende did contain hematite or goethite, these almost certainly would be mostly preterrestrial minerals produced during metasomatism within the first few tens of Ma of solar system formation.*

It is thought that pyrrhotite dominates the interior NRM for three reasons: (a) the NRM is blocked almost entirely below 290°C, similar to the NRM blocking temperature spectrum of sulfide-rich separates but not to that of sulfide-poor separates (Fig. 5 of ref. 11); (b) during thermal demagnetization,

~80% of saturation IRM of bulk samples is removed by 320°C (Fig. S4I and Fig. 7 of ref. 11), similar to that of sulfide-rich separates, but not sulfide-poor separates (which demagnetize only by ~12% by this temperature); (c) ~50% of ARM is thermally demagnetized by 330°C (Fig. 13 of ref. 4) and (d) the NRM has very high coercivity (with significant remanence blocked >290 mT), which is characteristic of pyrrhotite but not magnetite or metal (92, 93).

The average crystal size of the ferromagnetic minerals as inferred from previously published hysteresis data (4-8, 25, 94) is in the pseudo single domain to multidomain size range (following refs. 79, 95) (Fig. S5). To verify this, we measured our own hysteresis loops at room temperature on two samples (Fig. S5). Measurements were acquired with a Digital Measurement Systems VSM in the laboratory of C. Ross at MIT. The high-field slope (above 0.6 T) of each hysteresis loop was used to estimate the contribution of paramagnetic minerals. This contribution has been subtracted from the loops shown as dashed lines in Fig S5. Ratios of saturation remanence to saturation magnetization ( $M_{rs}/M_s$ ) and coercivity of remanence to coercivity ( $H_{cr}/H_c$ ) (where  $H_{cr}$  was measured using back-field IRM experiments) are characteristic of mean grain size of pseudo single domain with a possible contribution from superparamagnetic grains (79). Because magnetite dominates the rock magnetic properties [as shown by its dominance of many thermomagnetic curves (4, 11)], this grain size is mainly reflective of magnetite. Indeed, memory ratios for low-temperature cycling (see Section 4 and Fig. S8) are consistent with the magnetite being in the pseudo single domain size range (following ref. 96). The fact that there is less than 1% memory lost across the 34 K transition qualitatively indicates that pyrrhotite is very fine-grained. We cannot obtain a precise pyrrhotite grain size following ref. 97 because of the dominant presence of magnetite.

**4. Stability of early solar system remanence:** As described in the main text and Section 6, geochronometry indicates that Allende's paleomagnetic record should have originated in the very early solar system. Over the intervening 4.5 billion years (Ga), the meteorite experienced space temperatures determined by equilibrium with solar insolation and then landed on the Earth in 1969 in the Mexican state of Chihuahua. Our fusion crust baked contact test (see Section 1) alone essentially rules out terrestrial viscous remanent magnetization (VRM) as the main

source of the meteorite's MT component. Nevertheless, it is important to quantify how much of the NRM components were acquired as a VRM in the Earth's field since landing or alternatively were viscously modified while in space.

*Theoretical blocking temperature constraints.* Blocking temperature relations for single domain pyrrhotite (98, 99) and magnetite (100) indicate that 40 years of Earth residence at 20°C on Earth should have remagnetized crystals with 1-h blocking temperatures of ~70°C and ~100°C for pyrrhotite and magnetite, respectively (Fig. S6). These temperatures should be regarded as approximate because the average ferromagnetic grain size in Allende is pseudo single domain. Although no blocking temperature relations are yet available for awaruite, it is likely to behave roughly similar to magnetite due to their similar Curie temperatures. Given the dominance of pyrrhotite's contribution to the NRM, this predicts that much of the LT magnetization with 1-h blocking temperatures below ~70°C may contain terrestrial VRM.

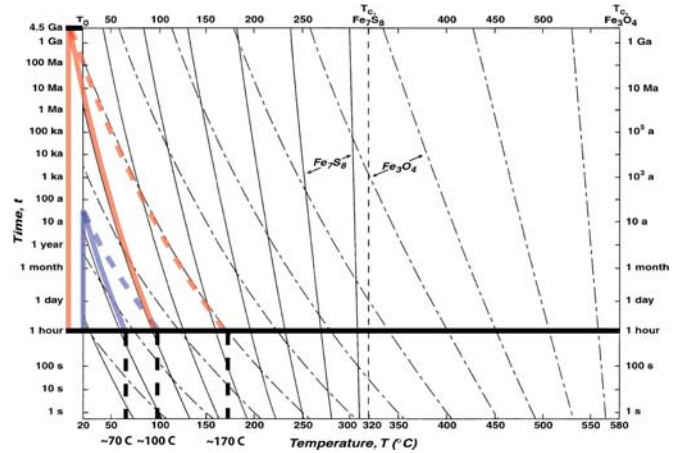


**Fig. S6.** Time-temperature remagnetization diagram for pyrrhotite ( $\text{Fe}_7\text{S}_8$ ) and magnetite ( $\text{Fe}_3\text{O}_4$ ) (after Fig.1 in ref. 99). Blocking or unblocking temperatures of magnetization for a particular ensemble of single-domain grains can be determined as a function of time by following one of the contours (98-100).

Another issue to consider is whether the observed NRM is theoretically stable over the 4.5 Ga history of the solar system. As described in the main text, our thermal demagnetization demonstrates that the LT, MT, and HT components are blocked up to ~190°C, between 190-290°C, and between 290-500°C, respectively. Thermal relaxation over 4.5 Ga at 0°C is predicted to demagnetize remanence carried by single domain pyrrhotite with 1-h blocking temperatures below ~100°C and by single domain magnetite below ~170°C (Fig. S6). Taken at face

value, these calculations indicate that the LT component is highly unlikely to be a record of early magnetism on the parent body history. This likely explains why the LT remanence unblocks much more rapidly than a TRM (compare blue and red curves in Fig. S4a-h). On the other hand, these calculations predict that the MT and HT components could be primary records of early solar system magnetism.

*Viscous remanent magnetization experiments.* To further constrain the origin of the NRM, we conducted laboratory VRM decay experiments (Fig. S7a). Three samples were exposed to the Earth's field ( $\sim 50 \mu\text{T}$ ) in a stationary position for 3 to 14 days and then brought into the shielded room ( $<150 \text{ nT}$ ). Beginning about 30 s after entry, their remanence was repeatedly measured over a time period up to the duration of the field exposure (Fig. S7a). In a second set of experiments, we also tracked the decrease of the remanence after acquisition of a VRM in a field of  $500 \mu\text{T}$  produced by a coil over time periods ranging from 100 s to three hours. We found that weak VRM (up to  $7 \times 10^{-6} \text{ Am}^2/\text{kg}$ , equivalent to 4% of the initial NRM) was acquired while we observed less than a  $20^\circ$  change in the magnetization direction.

These data allow us to constrain the rate of VRM acquisition. We found that data are well fit by assuming linear decay in  $\log(\text{time})$  for decay times  $> \sim 300 \text{ s}$ . This regime of approximate  $\log(\text{time})$  decay rate has been noted in many previous VRM experiment (101-103). Using a least squares regression to the data in Fig. S7a, we determined the magnetic viscosity decay coefficient  $S_d = d(\text{VRM lost})/d(\log \text{time}) = 1.38 \pm 0.20 \times 10^{-6} \text{ Am}^2/\text{kg}/\log(\text{s})$  ( $N = 6$ ) for a  $\sim 50 \mu\text{T}$  field.

Let us assume that our experiments can be extrapolated to longer timescales. Extrapolation to 40 years indicates that VRM acquired in the Earth's field since Allende's fall could likely account for no more than 1% of the observed NRM following storage in our magnetically shielded room for  $\sim 4$  months, in agreement with previous values (104).

Because VRM acquisition is approximately proportional to field intensity in the low-field limit, a bold extrapolation to 4.5 Ga suggests that if the LT component (which represents  $\sim 60\%$  of NRM) were a VRM acquired on the parent body in a large scale crustal field over solar system history, this field would have to be  $> \sim 300 \mu\text{T}$ . This is probably an upper limit given that the rock was likely much cooler

during these 4.5 Ga than it was during our VRM experiments.

These results are consistent with those predicted from fits using Richter's model for VRM acquisition [equation (3) of (101)] assuming a uniform unblocking time distribution with very large maximum unblocking times. However, the restricted duration times of our experiments mean that the VRM acquisition behavior at times much longer than our experimental time is essentially unconstrained by fits using Richter's model (even under the assumption of a grain size distribution, which itself cannot be independently verified).

Therefore, we have based our conclusion on the previously described fits for  $S_d$ . Because 40 years of Earth exposure is only 3  $\log(t)$  units larger than our experiment time, our conclusion that terrestrial VRM cannot explain the MT component is probably robust given how little VRM was acquired during our experiments. On the other hand, extrapolation of our VRM decay experiments over 4.5 Ga of solar system history is clearly much more hazardous.

*Effect of prolonged heating on maximum blocking temperatures of NRM.* Let us assume that the peak unblocking temperature of the MT component was set by the peak temperature of thermal metamorphism. In this case, it is possible that the prolonged ( $\sim$ several Ma) timing of thermal metamorphism might mean that the inferred peak temperature of  $290^\circ\text{C}$  is an overestimate because it was derived from laboratory 1-h blocking temperatures. In fact, the blocking temperature relations for pyrrhotite (Fig. S6), which is the mineral that dominates blocking below  $\sim 300^\circ\text{C}$ , show that even if the meteorite were held at  $290^\circ\text{C}$  for the age of the solar system, pyrrhotite grains with 1-h blocking temperatures of more than a few degrees above this value would not acquire NRM. This is because the blocking curves in this region of the diagram are essentially vertical. Magnetite's curves have shallower slope in this region but magnetite in Allende contributes  $<10\%$  to Allende's NRM and IRM below  $290^\circ\text{C}$ . Therefore,  $290^\circ\text{C}$  is likely a good estimate of the peak metamorphic temperature of Allende.

*Magnetostatic interaction experiments and implications for LT component.* The Earth's field is apparently too weak to explain the LT component as terrestrial VRM. To determine whether the LT component could instead be acquired as a VRM in the fine-scale interaction fields produce by nearby grains carrying the MT component over the last 4.5 Ga, we thermally demagnetized the LT components

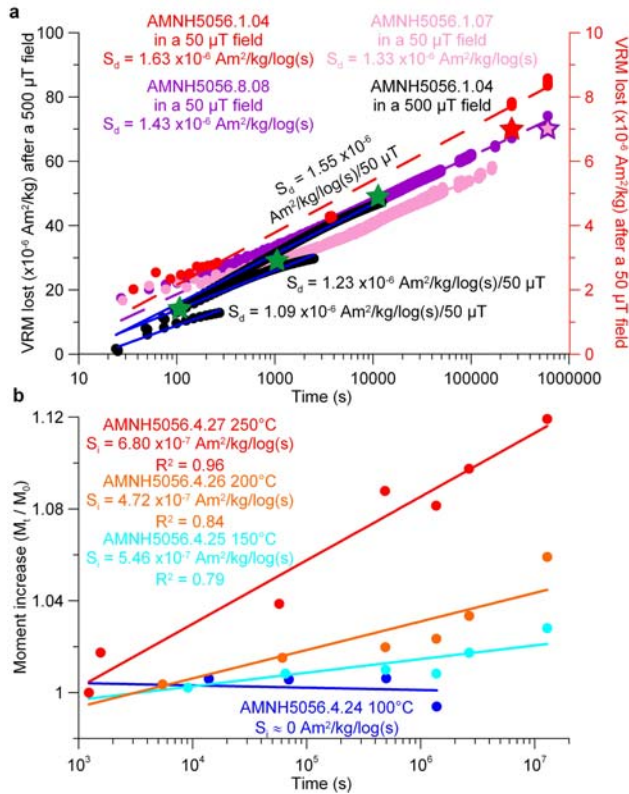


**Fig. S7. a**, VRM experiments on three subsamples. Samples were stored during 3, 7 and 14 days (given by red, pink and purple stars, respectively) in the Earth's magnetic field ( $\sim 50 \mu\text{T}$ ) and then returned to our shielded room ( $< 150 \text{ nT}$ ) where the moments were semi-continuously measured (in red, pink and purple circles, respectively). We used this to estimate the magnetic viscosity decay coefficient  $S_d$  using a least squares regression. One of these samples was then exposed to a  $500 \mu\text{T}$  dc field for a duration of 117, 1061 and 11,300 s (three green stars) and the decay of the resulting VRMs measured (three sets of black circles). **b**, Magnetostatic interaction experiments on four subsamples. Samples were thermally demagnetized to various temperatures and continually stored in a low field environment at room temperature. Their moments were measured after immediately cooling down ( $\sim 20$  min after peak temperature) as well as repeatedly thereafter over a period of 6 months. Samples were heated to a maximum temperature of  $100^\circ\text{C}$  (light blue),  $150^\circ\text{C}$  for (deep blue),  $200^\circ\text{C}$  (orange) and  $250^\circ\text{C}$  (red). The remaining NRMs immediately after thermal demagnetization are, respectively, 90, 60, 27 and 14% of the preheating NRMs. The magnetostatic interaction remagnetization coefficients  $S_i$  were estimated using a least squares regression.

of four new samples to various temperatures ( $100$ ,  $150$ ,  $200$  and  $250^\circ\text{C}$ ) and then repeatedly measured their remanence while they were stored in our shielded room ( $< 150 \text{ nT}$ ) over nearly five months (except for the  $100^\circ\text{C}$  sample which were not remeasured after a couple weeks) (Fig. S7b). For our  $100^\circ\text{C}$  demagnetization experiment, we observed no measurable moment variation other than the initial 10% drop caused by the heating itself. For the other three samples, we found that a weak remanence (up

to  $3 \times 10^{-6} \text{ Am}^2/\text{kg}$ , equivalent to 1.6% of the initial NRM) was slowly acquired along the direction of the MT component. The rate of this magnetostatic interaction acquisition is positively correlated with the amount of remanence initially thermally demagnetized (i.e., peak demagnetization temperature).

This is a strong indication that the samples acquired remanence in the interaction field produced by the remaining undemagnetized remanence. In particular, the positive correlation between demagnetization temperature and VRM acquisition can be explained by the fact that with increasing demagnetization temperature, there is an increasing quantity of demagnetized magnetic grains available to be remagnetized by the interaction fields of grains not demagnetized. Therefore, the LT component could have been acquired as the original NRM viscously demagnetized over the last 4.5 Ga and was replaced by this interaction remanence.

However, note that because there is virtually no magnetization blocked above  $290^\circ\text{C}$  in Allende, the MT component cannot itself be the product of small-scale interaction fields. This is because there is a competing effect that should become important for higher demagnetization temperatures: as the amount of demagnetization increases, the quantity of grains available to generate interaction fields will decrease. Thus, the rate of magnetostatic interaction acquisition should start to decrease above a certain unknown temperature. To demonstrate this, we remeasured the moments of 9 samples that had been previously (several months before) thermally demagnetized to  $320$ ,  $330$ ,  $380$  or  $580^\circ\text{C}$ . We found that the moments of these samples were within error or else 0.5% weaker than their moments measured immediately after the last thermal demagnetization step months earlier.

From the data in Fig. S7b, we estimated the magnetostatic interaction remagnetization coefficient  $S_i = d(\text{NRM gain})/d(\log \text{ time}) = 6.8 \times 10^{-7} \text{ Am}^2/\text{kg}/\log(\text{s})$  at  $20^\circ\text{C}$  for subsample 4.27 (which was heated up to  $250^\circ\text{C}$ ). This is a lower bound on the largest possible  $S_i$  during the last 4.5 Ga because  $250^\circ\text{C}$  is unlikely to be the optimum demagnetization temperature for maximizing the magnetostatic interaction remagnetization coefficient with respect to the two competing processes described above. Boldly extrapolating over 4.5 Ga, this would indicate that the minimum magnetostatic interaction remagnetization is of the order of  $1.2 \times 10^{-5} \text{ Am}^2/\text{kg}$ , equivalent to  $> \sim 11\%$  of the LT component. Thus, small-scale magnetostatic interactions were likely



more important than any terrestrial VRM and likely contributed to the LT component whose direction could have been controlled by the direction of the MT component. This conclusion must be viewed as provisional given the unknown temperature history of the rock and that we are extrapolating these experiments into deep time.

*Inverse TRM (ITRM).* Another issue that should be addressed is whether the magnetite-bearing NRM could be partially remagnetized or demagnetized during past temperature excursions across the  $\sim 120$  K Verwey transition of magnetite (105, 106). When warming up through this temperature in the presence of a magnetic field, magnetite can acquire an ITRM (107).

To address this possibility as well as further characterize the ferromagnetic mineralogy of Allende, we conducted two experiments for each of two subsamples: low temperature cycling of room temperature saturation IRM and thermal demagnetization of low temperature saturation IRM. In the first experiment (purple and pink curves in Fig. S8), samples were first exposed to a saturating (2.5 T) field at room temperature and then their moments were continuously measured while the samples were cycled in a weak field ( $< 200 \mu\text{T}$ , the minimum field in our MPMS) down to low temperature and back up to room temperature. In the second experiment (orange and grey curves in Fig. S8), samples were briefly exposed to a saturating (2.5 T) field at 10 K and then warmed up in a weak ( $< 200 \mu\text{T}$ ) field. The latter sequence was conducted twice for each sample: first after cooling in a near-zero ( $\sim 200 \mu\text{T}$ ) field and the second after cooling in a strong (2.5 T) field (110). Both experiments observed a soft Verwey transition, in general agreement with previous investigators (5, 8). However, the derivatives of the moment-temperature data with respect to temperature from both experiments show an apparent Verwey transition at  $\sim 105$ – $115$  K. The soft nature and reduced temperature of the transition are indicative of non-stoichiometric magnetite (105, 106), consistent with compositional measurements for Allende magnetite (4, 19, 68). Our low temperature cycling of IRM observed memory ratios of 63% and 86% at 300 K, substantially less than that previously observed for NRM cycling (4, 10, 94). Memory ratios are identical after the 75 K low temperature cycling, which shows that magnetite dominates the saturation IRM and that the splitting between the cooling and warming curves is due almost entirely to the Verwey transition (and not to the 34 K transition). These

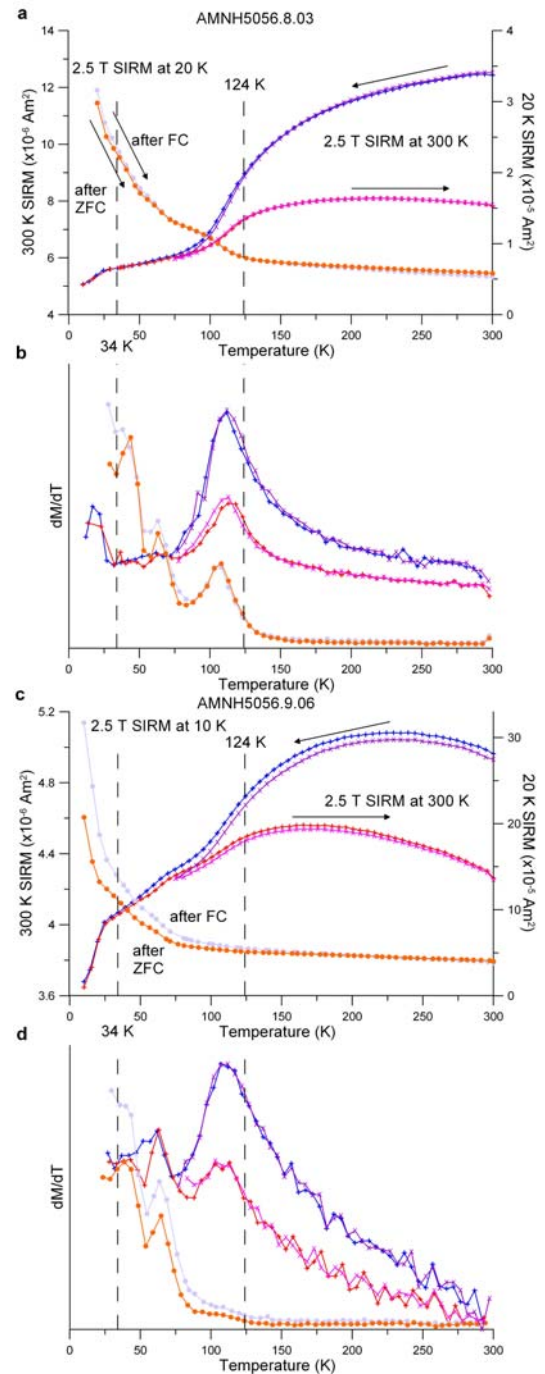


**Fig. S8.** Low temperature magnetometry experiments on two Allende interior subsamples. **a, c,** Continuous measurements of IRM (2.5 T applied at 300 K) during zero-field ( $< 200 \mu\text{T}$ ) cooling (300 K to 10 K shown by dark blue curve and 300 K to 75 K shown by red curve and 75 K to 300 K shown by light purple curve) and of low temperature IRM (2.5 T was applied at 20 K) during warming (20 K to 300 K) after zero-field ( $< 200 \mu\text{T}$ ) cooling (ZFC, shown by orange curve) and field cooling (FC, shown by light blue curve). **b, d,** Derivative of the remanence curves in (**a, c**) using same color scheme. Pyrrhotite's 34 K monoclinic transition (108, 109) and stoichiometric magnetite's 124 K Verwey transition (105, 106) are shown as black dashed lines.

memory ratios indicate that the magnetite has an average crystal size in the pseudo single domain field.

The derivative curves for the second experiment exhibit additional peaks at  $\sim 35$ -40 K and  $\sim 65$  K. The former is likely a signature of monoclinic pyrrhotite (108, 109), while the latter may be a reflection of troilite or kamacite (111). The second but not the first sample possesses a continuous opening between FC and ZFC curves (Fig. S8c, d), which may reflect a small quantity of goethite, as also possibly indicated by some microprobe (73) and Mössbauer data (87). The fact that the moment variations at the Verwey transition are far greater than those at the 34 K transition indicates that magnetite dominates the rock magnetic properties of Allende, implying that we cannot obtain a precise pyrrhotite grain size. This dominance of magnetite is also indicated by thermomagnetic curves (4, 11), as mentioned in Section 3.

These data as well as a consideration of Allende's likely thermal history lead us to conclude that any effects on the meteorite's NRM from low temperature transitions must be modest. Because at least  $\sim 90\%$  of Allende's NRM is carried by pyrrhotite, low temperature magnetization processes can only have affected at most  $\sim 10\%$  of the remanence carrying capacity of the meteorite. If Allende had ever cycled below 77 K, then the observed IRM memory ratios would suggest only 5-8% of the NRM would have been affected. Furthermore, the fact that the HC component is blocked up to 290 mT indicates the MT component is unlikely to be mostly an ITRM, which has been found to be blocked generally by grains with much lower coercivities (107).

In any case, it is unlikely that the meteorite ever reached such low temperatures, which would have required it to have originated in the outer asteroid belt (where the disk-averaged equilibrium blackbody temperature of fast-rotating objects approaches  $\sim 120$  K) or beyond, on a very slowly rotating body, or in a permanently shadowed crater or the polar region of a larger body. Even if Allende was at one time below this temperature, it should have warmed up through the transition as it continuously reequilibrated with solar insolation during slow orbital migration, which is thought to take at least 100,000 years in even the fastest meteorite transfer scenarios from the asteroid belt (112) [note that Allende's exposure age is  $\sim 5$  million years (Ma) (113)]. Thus even the center of a several meter-diameter meteoroid from the outer asteroid belt would therefore have warmed through

the 120 K equilibrium temperature long before it entered the inner solar system. Given that nearly all of interplanetary space contains very weak magnetic fields ( $< 10$  nT), this means that Allende magnetite would have been demagnetized, not magnetized, by such an event.

We conclude that the stable early solar system MT component should have been well preserved while the LT component is likely the result of strong crustal and/or fine-scale magnetostatic interaction fields.

**5. Paleointensities:** We conducted paleointensity experiments using both Thellier-Thellier and AF methods (12).

*Thellier-Thellier paleointensities.* We conducted the IZZI variant [alternating zero-field (Z) and in-field (I) measurements] (114-119) of the Thellier-Thellier paleointensity experiment on four subsamples (Fig. S9). These incorporated pTRM checks for alteration and pTRM tail checks for multidomain (MD) behaviour.

As a control, we also conducted the same experiment on a tholeiitic basalt sample (B0829-1.E1) from the Hawaii Scientific Drilling Project 2 (HSDP2) core (120). This 53 mg sample was drawn from an undemagnetized endchip of the 25-mm diameter sample B0829-1 described in ref. 121. Our pTRM check-corrected (122-126) paleointensity for the terrestrial control sample is  $29.7 \pm 0.5$   $\mu$ T (Table S2 and Fig. S9j), which is within error of previous Thellier-Thellier values obtained from the HSDP2 core [ $29.5 \pm 1.4$   $\mu$ T for  $N = 2$  "Class A" samples from core depth 2416.5 m, about 5 m from our sample] (127). Nevertheless, our sample's paleointensity experiment fails the standard "Class A" criteria (125). The agreement with previous values despite this failure is exemplary of how useful paleointensities can sometimes still be derived from experiments that fail strict quality criteria.

Both our raw and our alteration-corrected (122-126) Arai diagrams for Allende (Table S2 and Fig. S9b, d, f, h) reveal three slope segments corresponding to three different magnetic field intensities (Figs. 3 and S9). These three paleointensities are directly correlated with the LT (up to  $230^\circ\text{C}$ ), MT ( $200$ - $290^\circ\text{C}$ ), and HT ( $> 290^\circ\text{C}$ ) components as identified by changes in NRM direction during demagnetization (Figs. 1-2 and S3-S4). Unlike previous investigators (4, 29), our relatively high resolution thermal demagnetization schedule allowed us to demonstrate that the MT component is distinct from the LT component in both direction and paleointensity. For the

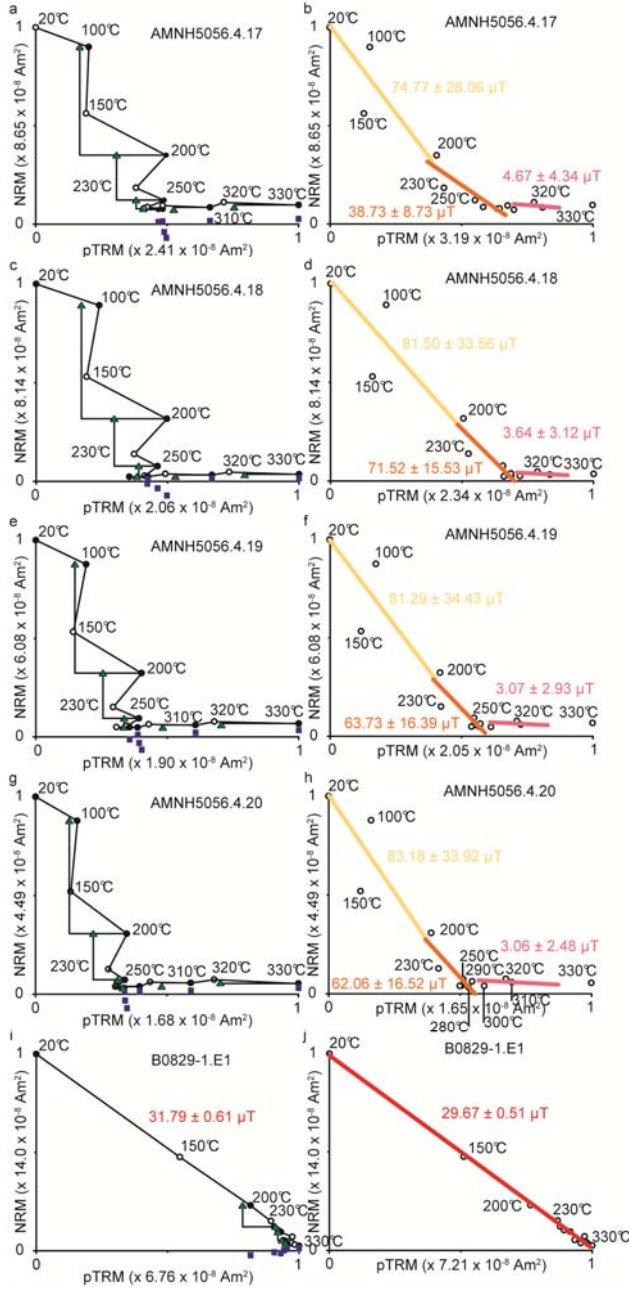


**Fig. S9.** Thellier-Thellier palaeointensity experiments for AMNH5056 subsamples and a control terrestrial basalt following the IZZI variant [alternating zero-field (Z) and in-field (I) measurements]. Closed and open symbols represent respectively ZI and IZ steps, respectively. Peak temperatures for selected steps are shown. (a, c, e, g, i) Arai plots displaying the pTRM checks (triangles) for alteration and the pTRM tail checks (squares) for multidomain behaviour. (b, d, f, h, j) Arai plots corrected for alteration revealing palaeointensities for the LT (yellow), MT (orange) and HT (pink) linear segments. (a, b) Sample 4.17. (c, d) Sample 4.18. (e, f) Sample 4.19. (g, h) Sample 4.20. (i, j) Control sample: Hawaiian basalt B0829-1.E1.

HT magnetization ( $>290^{\circ}\text{C}$ ), we found a nearly horizontal segment (essentially within error of zero) in

the Arai plot indicative of very weak ( $<4\text{ }\mu\text{T}$ ) paleointensities.

Our alteration-corrected Thellier-Thellier experiments for the MT component yielded paleointensities of  $59.0 \pm 14.1\text{ }\mu\text{T}$  (range is 1 standard deviation for 4 samples) (Table S2 and Figs. 3 and S9). Without alteration correct, the mean MT paleointensity is even stronger  $123.0 \pm 11.2\text{ }\mu\text{T}$ . Previously published Thellier-Thellier paleointensities are about twice that of our alteration-corrected MT component values and are instead close to our LT component and alteration-corrected MT component values (4, 9, 28, 29). The agreement with our LT component values is expected because the heating schedules of these previous studies had lower temperature resolution and/or lower peak heating temperatures, which meant that they were mainly characterizing the LT component.

*Thellier-Thellier uncertainties.* Like our basalt control sample and most extraterrestrial samples, all of our Allende experiments fail most standard quality criteria, mainly due to alteration (as quantified by the pTRM checks) and MD-like behaviour (as quantified by the pTRM tail checks and zigzagging between IZ and ZI steps in the Arai diagrams). Of course, these criteria were derived from decades of work with terrestrial samples that usually have more thermally stable mineralogy and more single-domain-like magnetic properties than extraterrestrial rocks. This indicates that our Allende Thellier-Thellier values have higher uncertainties relative to successful Thellier-Thellier paleointensities for terrestrial samples, which can sometimes achieve  $>10\%$  accuracy. The quality criteria do not easily allow the user to quantify paleointensity uncertainties. As a result, they are typically used to make a somewhat arbitrary designation of pass or failure for a particular sample.

Probably the most direct way to establish the accuracy of the paleointensity values is to conduct a repeat paleointensity experiment on a laboratory TRM (118, 128). With this goal, seven samples were given a laboratory  $320^{\circ}\text{C}$  pTRM acquired during cooling in a field of  $48.5\text{ }\mu\text{T}$ . In order to determine the effect of prior sample alteration on the recovered paleointensity values, four of these samples had previously been subjected to the NRM IZZI paleointensity protocol, while the remaining three samples were pristine. We then conducted new paleointensity experiments on the seven samples following a similar protocol to that used to characterize the NRM (Fig. S10a-g). In these experiments, we re-



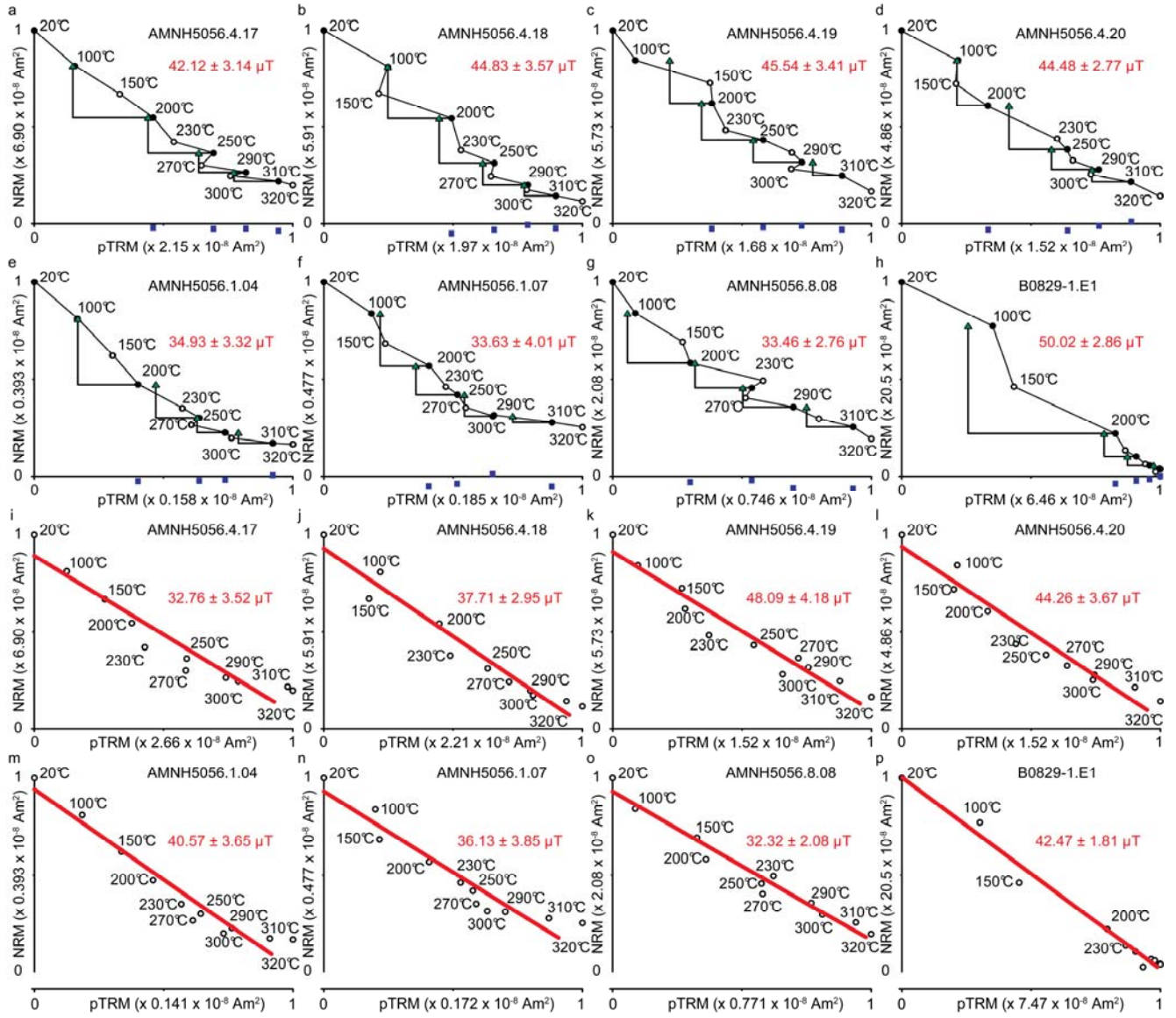


**Fig. S10.** Synthetic Thellier-Thellier palaeointensity on subsamples from AMNH5056 following the IZZI variant (alternating zero-field (Z) and in-field (I) measurements) on a pTRM acquired during 20 min cooling from 320°C in a field of 48.5  $\mu\text{T}$  perpendicular to that used for the palaeointensity determination. **(a-h)** Arai plots (ZI = closed symbols and IZ = open symbols) displaying the pTRM checks (triangles) for alteration and the pTRM tail checks (squares) for multidomain behaviour. **(i-p)** Arai plots corrected for alteration revealing linear trends. Samples **(a, i)** 4.17, **(b, j)** 4.18, **(c, k)** 4.19 and **(d, l)** 4.20 were previously thermally demagnetized during the NRM palaeointensity experiments. Samples **(e, m)** 1.04, **(f, n)** 1.07, **(g, o)** 8.08 were previously demagnetized by alternating field treatment. The reference sample **(h, p)** B0829-1.E1 assess the fidelity of our experiments.



Label	$T_{\min}$ (°C)	$T_{\max}$ (°C)	$N$	$\beta$	$f$	$g$	$q$	MAD (°)	dANG (°)	$\delta(TR)$	$B_{corr}$ ( $\mu T$ )	Std. Dev.	$B_{uncorr}$ ( $\mu T$ )	Std. Dev.	$B_{mean}$ ( $\mu T$ )
Natural remanent magnetization															
4.17LT	0	200	4	0.38	0.68	0.62	1.1	2.7	9.2	5.7	74.77	28.06	82.21	28.69	<b>80.19 ± 3.71</b>
4.18LT	0	200	4	0.41	0.71	0.62	1.1	2.6	5.5	6.7	81.50	33.56	81.50	33.56	
4.19LT	0	200	4	0.42	0.71	0.6	1	3.5	6.6	5.9	81.29	34.43	81.29	34.43	
4.20LT	0	200	4	0.41	0.72	0.62	1.1	1.9	6.7	6.6	83.18	33.92	83.18	33.92	
4.17MT	200	290	7	0.23	0.41	0.74	1.4	4.3	11.5	8.8	38.73	8.73	125.61	88.18	<b>59.01 ± 14.13</b>
4.18MT	200	290	7	0.22	0.31	0.67	1	3.7	3.6	7.3	71.52	15.53	136.24	108.99	
4.19MT	200	290	7	0.26	0.33	0.66	0.8	4.4	6.9	7.1	63.73	16.39	120.66	87.78	
4.20MT	200	290	7	0.27	0.34	0.65	0.8	3.7	6.1	8.2	62.06	16.52	109.34	70.01	
4.17HT	290	330	5	0.93	0.11	-1.38	0.2	14.9	110.3	32.1	4.67	4.34	3.66	3.64	<b>3.61 ± 0.76</b>
4.18HT	290	330	5	0.86	0.14	-1.22	0.2	20.3	106.3	74.8	3.64	3.12	2.25	2.18	
4.19HT	290	330	5	0.95	0.13	-1.09	0.1	19.4	110.7	52.9	3.07	2.93	2.27	2.32	
4.20HT	290	330	5	0.81	0.2	-0.66	0.2	17.5	126.5	61.7	3.06	2.48	2.20	2.00	
B0829-1.E1	0	330	13	0.02	0.98	0.65	37.5	1.2	1.9	1.3	29.67	0.51	31.79	0.61	
Laboratory partial thermoremanence															
4.17	0	320	11	0.11	0.84	0.88	6.9	3.9	11.6	1.9	32.76	3.52	42.12	3.14	<b>38.83 ± 5.86</b>
4.18	0	320	11	0.08	0.92	0.87	10.2	1.7	5.0	3.8	37.71	2.95	44.83	3.57	
4.19	0	320	11	0.09	0.86	0.87	8.6	2.7	8.0	1.7	48.09	4.18	45.54	3.41	
4.20	0	320	11	0.08	0.9	0.88	9.5	3.1	5.7	1.5	44.26	3.67	44.48	2.77	
1.04	0	320	11	0.09	0.91	0.86	8.6	2.8	6.6	2.4	40.57	3.65	34.93	3.32	
1.07	0	320	11	0.11	0.81	0.86	6.5	6.4	7.6	2.5	36.13	3.85	33.63	4.01	
8.08	0	320	11	0.06	0.81	0.86	10.8	4.6	5.8	3.4	32.32	2.08	33.46	2.76	
B0829-1.E1	0	320	11	0.04	0.98	0.77	17.7	2.0	2.1	2.6	42.47	1.81	50.02	2.86	

**Table S2.** Shown are our paleointensity results using the IZZI variant of the Thellier-Thellier technique. The top and bottom portions of the table present paleointensity data for the NRM and laboratory induced 320°C pTRM acquired in a 48.5  $\mu T$  field, respectively (see Section 5). The first column gives the subsample name, and  $T_{\min}$  and  $T_{\max}$  in columns two and three give the range of temperature in which the  $N$  consecutive points (column four) were used for the regression line. Columns five through eight give the pTRM check-corrected scatter parameter ( $\beta$ ) and the fraction ( $f$ ), gap ( $g$ ) and quality ( $q$ ) factors (125). Columns nine and ten give the maximum angular deviation (MAD) and difference angle (dANG) from the principal component analyses (48). Columns eleven  $\delta(TR)$  quantify the pTRM tail check. Columns twelve and thirteen give the alteration-corrected paleointensity estimates ( $B_{corr}$ ) with their standard deviations from the regression line. Columns fourteen and fifteen give the uncorrected paleointensity estimates ( $B_{uncorr}$ ) with their standard deviations from the regression line. Column sixteen gives the mean paleointensity determinations ( $B_{mean}$ ) with their standard deviations (calculated as the dispersion of the data in the  $B_{corr}$  column). The laboratory field for all experiments was 15.6  $\mu T$ .

covered a paleointensity of  $38.8 \pm 5.9 \mu\text{T}$  for the Allende samples ( $N = 7$ ), within 80% of the laboratory field. Again, these experiments fail many of the “Class A” criteria (125) due to sample alteration and MD-like behaviour (e.g., zigzagging, concave Arai plots). There is no difference in mean paleointensities derived from the four previously heated samples versus the pristine samples, indicating that the results are not strongly controlled by the amount of alteration occurring during the experiments. These results strongly indicate that our Thellier-Thellier paleointensities on Allende’s MT component have uncertainties of a factor of only  $\sim 2$ . This uncertainty, although large by the standards of terrestrial paleomagnetism, is far more than sufficient for distinguishing between various hypothesized field sources in the early solar system (Fig. 3).

**AF paleointensities.** Our AF paleointensity experiments used either anhysteretic remanent magnetization (ARM) in a 200 mT ac field with three different dc bias fields (12) (50, 200 and 600  $\mu\text{T}$ ) or else saturation IRM (0.9 T) as the normalizing quantity (Figs. 3, S11 and S12). Multicomponent paleointensity estimates were obtained from plots of NRM lost versus ARM gained and NRM lost versus IRM lost (see refs. 12, 46 for details). However, unlike all previous studies of Allende, we calibrated these AF paleointensities by measuring the average ratios of ARM to TRM  $f = 0.373 \pm 0.0814$  ( $N = 9$ ; 3 samples) and IRM to TRM  $f = 13,100 \pm 3,590$  ( $N = 6$ ; 3 samples) for grains with coercivities  $> 56$  mT (Fig. S11). The low  $f$  factor and high  $f$  factor are almost certainly attributed to the fact that only a fraction of the mineralogy is magnetized in the NRM or pTRM. The variation in the AF-corrected palaeointensity values for the three samples in Fig. S11 is about  $\sim 40\%$  even though all samples were originally cooled in the same 98.5  $\mu\text{T}$  laboratory field. This indicates that even with our calibration, the ARM and IRM palaeointensities in Figs. 3 and S12 likely have a factor of several uncertainties. Our results for the HC component ( $> 56$  mT) in interior subsamples gave values of  $61.2 \pm 13.1 \mu\text{T}$  after normalizing to ARM, and  $55.3 \pm 15.5 \mu\text{T}$  after normalizing to IRM (ranges are standard deviation of 59 and 30 experiments using the ARM and IRM methods, respectively) (Fig. 3).

These values agree with previous AF paleointensity estimates (5, 6, 11, 25) when the latter are also thermally calibrated using our ARM/TRM and

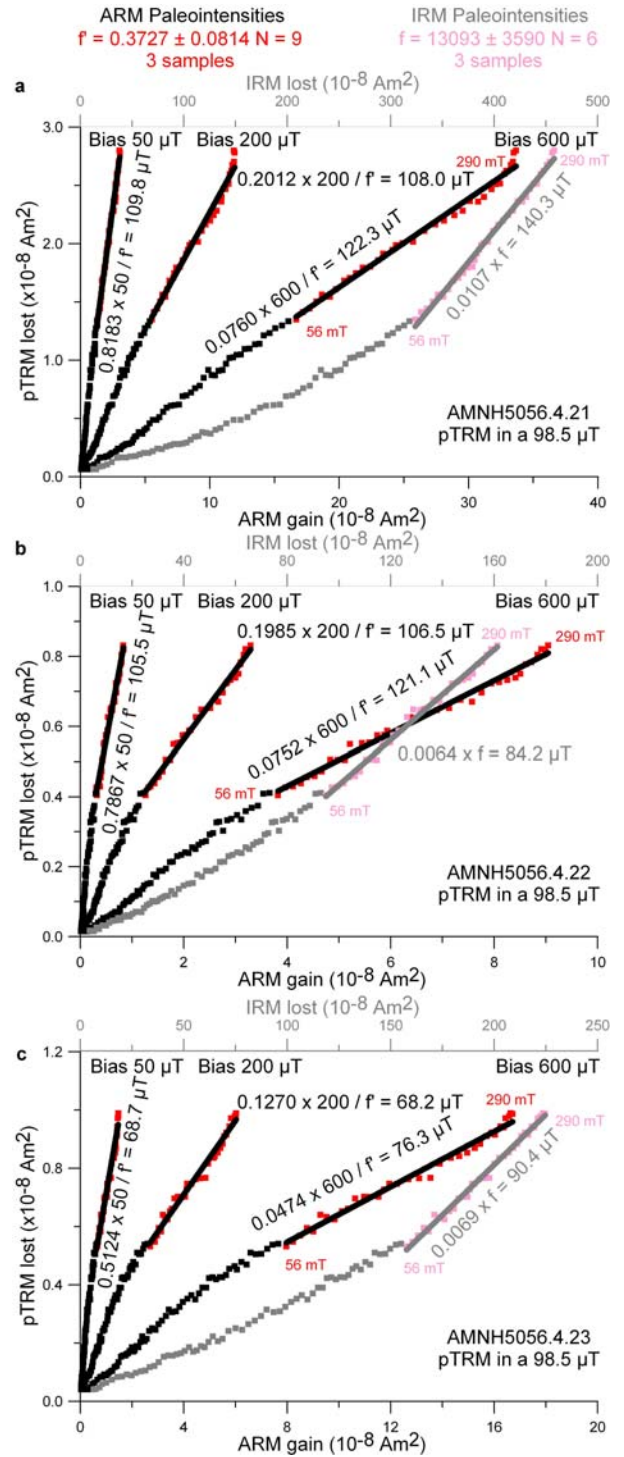


**Fig. S11.** Thermal calibration of AF paleointensity experiments. Samples were given a laboratory pTRM by cooling from 320°C in a field of 98.5  $\mu\text{T}$ . (a) sample 4.21. (b) sample 4.22. (c) sample 4.23. Data points from HC components used to compute paleointensities are coloured red/pink. ARM method, in which cumulative ARM acquired in laboratory dc bias fields of 50  $\mu\text{T}$ , 200  $\mu\text{T}$ , and 600  $\mu\text{T}$  superimposed on stepwise increasing AF is plotted in black as a function of remanence lost during AF demagnetization. Paleointensity in microteslas =  $(\text{pTRM}/\text{ARM})/f \times (\text{bias field in microteslas})$ , with the average factor  $f = 0.373 \pm 0.081$  ( $N = 9$ ). IRM method, in which cumulative AF demagnetization of a saturat-

ing IRM is plotted in grey as a function of AF demagnetization of the remanence. Palaeointensity in microteslas =  $p\text{TRM}/\text{IRM} \times f$ , with the average factor  $f = 13,100 \pm 360$  ( $N = 6$ ) (slope and REM' method for three samples).

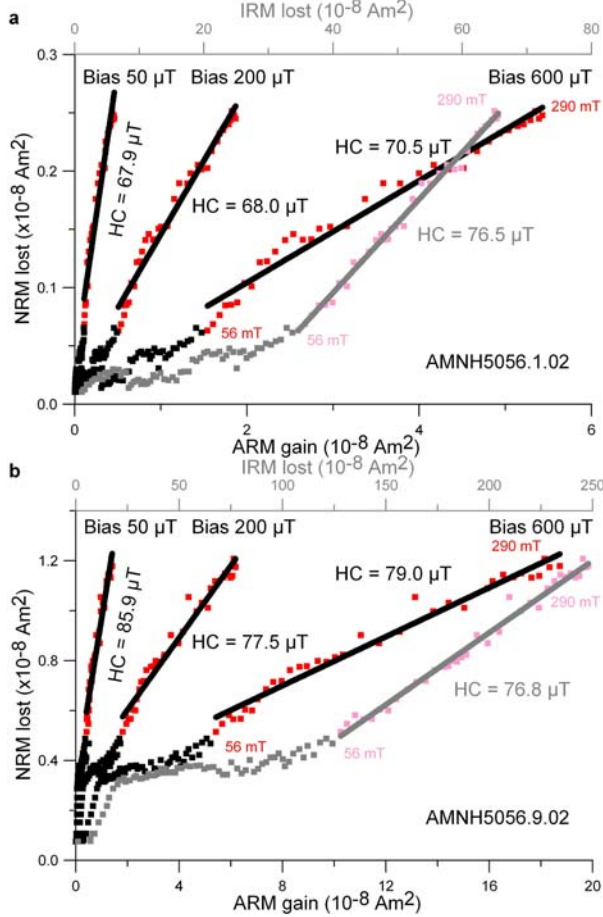


**Fig. S12.** AF palaeointensity experiments for (a) sample 1.02 and (b) sample 9.02. Data points from HC components are coloured red/pink. ARM method, in which cumulative ARM acquired in laboratory dc bias fields of 50  $\mu\text{T}$ , 200  $\mu\text{T}$ , and 600  $\mu\text{T}$  superimposed on stepwise increasing AF is plotted in black as a function of remanence lost during AF demagnetization. For sample 1.02, the HC component is estimated to have been acquired in a palaeofield of 67.9  $\mu\text{T}$  (50  $\mu\text{T}$  bias field), 68.0  $\mu\text{T}$  (200  $\mu\text{T}$  bias field), and 70.5  $\mu\text{T}$  (600  $\mu\text{T}$  bias field). For sample 9.02, the HC component is estimated to have been acquired in a palaeofield of 85.9  $\mu\text{T}$  (50  $\mu\text{T}$  bias field), 77.5  $\mu\text{T}$  (200  $\mu\text{T}$  bias field), and 79.0  $\mu\text{T}$  (600  $\mu\text{T}$  bias field). IRM method, in which cumulative AF demagnetization of a saturating IRM is plotted in grey as a function of AF demagnetization of the remanence. The HC component is estimated to have been acquired in a palaeofield of 76.5  $\mu\text{T}$  for sample 1.02 and in a palaeofield of 76.8  $\mu\text{T}$  for sample 9.02.

IRM/TRM measurements. They are also within error of our Thellier-Thellier paleointensities from the MT component.

**Summary.** Both the Thellier-Thellier and AF paleointensity data strongly indicate that the MT component was acquired in fields of at least of order 60  $\mu\text{T}$  (Figs. 3 and S9). If we consider a

cooling rate correction (129) (68% overestimation determined by comparing our 1-h laboratory heating schedule to the 1 Ma inferred metamorphism timescale; see main text and Section 6), and the factor of  $\sim 2$  estimated measurement uncertainty (for AF paleointensities, the observed sample-to-sample variation in measured TRM/ARM and TRM/IRM and for Thellier-Thellier paleointensities,  $\sim 2$  standard deviation scatter), a minimum value of 20  $\mu\text{T}$  is indicated. If the NRM were a TCRM, these values would likely be lower limits given its usual inefficiency relative to TRM (130). Even in the unusual cases where TCRM may be stronger than TRM, paleointensities derived from TCRM have still been observed to be within several tens of percent of the true value (131). As discussed in the main text (e.g. Fig. 3), this strong  $\sim 20$   $\mu\text{T}$  minimum paleointensity values stringently constrains the source of the paleofield.

**6. Thermochronology:** The age of NRM acquisition and the time period over which it was acquired have critical implications for identifying the magnetizing field. Pb/Pb (13) and Al/Mg (14) chronometry indicate that chondrules in CV chondrites may be the oldest known for any chondrite class and could have been formed rapidly, possibly as short as 200,000 years (14), after calcium aluminum inclusion (CAI) formation and lasting for somewhere between 1.2-3 Ma, depending partly on the Pb/Pb age of CAIs (13, 132). However, most chondrules in Allende appear to have formed 1.7 Ma after CAIs (14). These ages set a maximum age for the magnetization. Al/Mg ages of secondary nepheline, sodalite, and grossular in Allende CAIs suggest that the last episode of aqueous alteration took place at least several half-lives of  $^{26}\text{Al}$  (i.e.,  $> 2$  Ma) after CAI formation (133). The persistence of primordial  $^{26}\text{Al}$  anomalies in unaltered CAI phases confirms that Allende cannot have experienced wholesale metamorphism over Ma timescales above  $\sim 500$ - $600^\circ\text{C}$  (134) since the formation of CAIs (135). The compositions of metal, sulfide, and oxide phases in Allende indicate prograde metamorphism at  $\sim 500^\circ\text{C}$  for  $> 10^3$ - $10^4$  years (19). Although we are aware of no Mn/Cr studies of secondary phases in Allende, Mn/Cr ages of secondary fayalite in chondrules and matrix in six other CV chondrites are  $\sim 5$ -8 Ma after CAIs (15, 136).

The Rb/Sr, U/Pb, Re/Os,  $^{40}\text{Ar}/^{39}\text{Ar}$ , and (U-Th)/He chronometers are disturbed but do not yield precise constraints on the post-accretional thermal

history of Allende.  $^{40}\text{Ar}/^{39}\text{Ar}$  chronometry yields complex age spectra (partly due to  $^{39}\text{Ar}$  recoil and trapped Ar) which suggest that most chondrules and refractory inclusions have ages of  $4.53 \pm 0.03$  Ga, essentially within error of the age of the solar system (137-140). Analysis of matrix samples and some chondrules and inclusions obtained younger ages ( $\sim 2$ -4 Ga) but the complexities of the age spectra do not permit quantitative thermal constraints (137, 141). Rb/Sr ages of bulk samples are, within error, indistinguishable of the age of the solar system, but many chondrules show evidence for a later disturbance whose temperature and time are difficult to quantify (142). Re/Os are also ancient but disturbed but in way difficult to quantify (143). (U-Th)/He ages of Allende chondrules and bulk samples are 4.2 and 3.4 Ga, respectively, with a nominal uncertainty of  $\pm 0.2$  Ga (144). These bulk sample ages might indicate a late disturbance, but the lithologic heterogeneity of the meteorite, the fine grain size of the matrix, the lack of alpha-ejection corrections, and the large amount of cosmogenic  $^4\text{He}$  make the thermal implications of this difficult to quantify.

Unlike the previously discussed long-lived chronometers, the short-lived I/Xe system (145, 146) has the potential to place constraints with sub-Ma precision on the formation, metamorphism, and thermal history of Allende. I/Xe dating has been applied to several components of Allende including CAIs, chondrules, dark inclusions (DIs) and host matrix (refs. 18, 147-151). The major carrier of radiogenic  $^{129}\text{Xe}$  ( $^{129}\text{Xe}^*$ ) in Allende is thought to be sodalite produced during metasomatism on the parent body (147, 150). These studies have revealed systematic differences between the apparent I/Xe closure ages of these components that have typically been quantified from Xe-Xe “isochron” or mixing diagrams calculated from sequentially degassed Xe. The closure ages of CAIs are  $\sim 3.1$  to  $\sim 4.2$  Ma younger than the Shallowater standard [whose absolute age is  $4562.3 \pm 0.4$  Ma (145)], chondrules are  $\sim 0.5$  to  $\sim 2$  Ma younger, and DIs are  $\sim 2.8$  to  $\sim 0.5$  Ma older. Since these differences presumably reflect the predominance of different  $^{129}\text{I}$ -containing phases within these components and may also reflect differences in their Xe retention properties, the I/Xe chronometer has been used to infer timescales of a complex and prolonged history over millions of years involving alteration and/or metamorphism on the chondrite parent

body, possibly involving aqueous chemistry at elevated temperatures (17, 18, 64, 147, 151).

Although ages are typically calculated from assumed isochronous mixing diagrams, it is also possible to calculate a Xe age spectrum (i.e., an apparent relative age for each step vs. the cumulative  $^{128}\text{Xe}$  release fraction) by assuming a common, trapped, non-radiogenic Xe component (147). A  $^{128}\text{Xe}$ -based age spectrum has the potential to resolve age differences between sub-component phases as “age plateaus” observed as sequential isochronous heating steps and can also constrain the spatial distribution of  $^{129}\text{Xe}^*$  within the analyzed sample. By assuming a trapped ordinary chondrite Xe “OC-Xe” component (152) [ $^{132}\text{Xe}/^{128}\text{Xe} = 12.09$  and  $^{129}\text{Xe}/^{128}\text{Xe} = 12.57$ ], existing CAI and chondrule datasets (149) reveal well-defined age plateaus over most of the released gas that are distinct from and typically younger than the most retentive sites observed at the highest temperature extractions (e.g., Fig. 4). These age spectra further suggest that the samples experienced metamorphic or aqueous disturbance after they formed, which resulted in the dominant age plateaus. Although the absolute extraction temperatures during these analyses are poorly known (147, 151), samples with high apparent Xe retentivity (i.e., which primarily release Xe at higher temperatures) tend to have the oldest relative ages (DIs), whereas the least Xe-retentive samples (CAIs) have the youngest plateau ages (147). The observed correlation between I/Xe ages and Xe extraction temperatures suggests that differences in Xe retentivity may have caused a divergence in I/Xe ages of these materials as a function of “closure” temperature and is at least qualitatively permissive of slow cooling metamorphism on the parent body.

It has been argued (147) that in one existing dataset of an Allende CAI (17), extraction temperatures were determined with sufficient precision and accuracy to calculate Xe diffusion coefficients as a function of temperature (Fig. 4a). This calculation (153) assumes an initially uniform spatial distribution of neutron-induced  $^{128}\text{Xe}$  ( $^{128}\text{Xe}^*$ ) produced synthetically from  $^{127}\text{I}$ . Other published analyses report insufficient temperature accuracy to quantify Xe diffusion kinetics (18, 147, 151). Assuming that the diffusion kinetics shown in Fig. 4a applies over all time and can be extrapolated to lower temperatures, we can predict the spatial distribution of  $^{129}\text{Xe}^*$  within a spherical diffusion domain for any



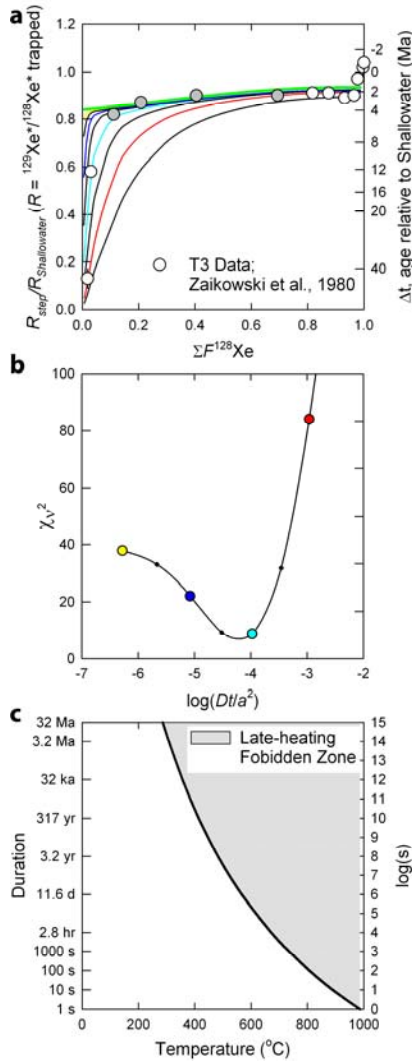


**Figure S13.** Constraining late-stage thermal conditions using  $^{129}\text{Xe}^*/^{128}\text{Xe}^*$  thermochronology of Allende CAI T3. (a) Measured and modeled  $^{129}\text{Xe}^*/^{128}\text{Xe}^*$  ratio evolution spectra for the T3 CAI including the 390°C thermal model shown in Fig. 4 (4 Ma event occurring between -0.5 and +3.5 Ma relative to Shallowater) and a second heating event at 4.36 Ga (142) (+203 Ma relative to Shallowater) using the same parameters and assumptions described in the Fig. 4 caption. (b) The reduced chi squared ( $\chi_v^2$ ) fit statistics for various model heating conditions at 4.36 Ga plotted versus values of  $\log(Dt/a^2)$ . The best-fit value of  $Dt/a^2$  for the late-stage heating is identified at the minimum  $\chi_v^2$  value. Colored points correspond to models shown in panel (a), small black points indicate explicitly modeled conditions, and curves are polynomial fits to the  $\chi_v^2$  values used to identify the minimum in  $Dt/a^2$ . (c) Duration-temperature constraints on a thermal excursion at 4.36 Ga. The solution set of duration and temperature combinations is shown as a curve of constant  $Dt/a^2$  identified at the minimum in panel (b). Since the diffusion kinetics used in this calculation place a lower bound on diffusivity applicable to the first two heating steps, the curve in (c) places a strong upper bound on the thermal conditions of the sample at that time. Since  $^{129}\text{I}$  is effectively extinct by 4.36 Ga, the upper bound also applies to all points in time after 4.36 Ga ago.

arbitrary thermal history using a numerical model. To test the possibility that the CAI resided at elevated temperatures over millions of years after CAI formation, we calculated model distributions of  $^{129}\text{Xe}^*$  and model release patterns of  $^{129}\text{Xe}^*/^{128}\text{Xe}^*$  for the thermal histories shown in Fig. 4b. These calculations predict patterns of  $^{129}\text{Xe}^*/^{128}\text{Xe}^*$  as a function of the cumulative  $^{128}\text{Xe}$  release fraction ( $\Sigma F^{128}\text{Xe}$ ) that can be compared against the observed data (Fig. 4c, d). Note that for observed data,  $^{129}\text{Xe}^*/^{128}\text{Xe}^*$  represents the apparent radiogenic  $^{129}\text{Xe}$  to  $^{128}\text{Xe}$  ratio after subtraction of the OC-Xe component (see above).

In this case, ~80% of the observed Xe plots along a well-defined age plateau of ~2.5 Ma after Shallowater (Fig. 4c, d), including ~50% of the gas comprising the linear Arrhenius relationship (Fig. 4a). Due to the apparently high activation energy of Xe diffusion in this material ( $289 \pm 16$  kJ/mol), these data tightly restrict acceptable thermal models assuming that the observed pattern of  $^{129}\text{Xe}^*/^{128}\text{Xe}^*$  vs.  $\Sigma F^{128}\text{Xe}$  (and the correspondingly inferred spatial distribution of  $^{129}\text{Xe}^*$ ) resulted solely from radiogenic in-growth and thermally activated diffusion. We find that the observed plateau is well explained by a mean temperature of a  $390 \pm 15^\circ\text{C}$  thermal event lasting from 0.5 Ma before to 3.5 Ma after the age of the Shallowater standard. These uncertainties are minimum estimates in that they are derived from formal regression errors only and do not include a contribution from the temperature extrapolation of the Arrhenius relationship. This temperature is remarkably close to the peak temperature constraints derived from the other petrologic, geochemical and paleomagnetic data (see main text).

The Allende CAI dataset (17) also contains evidence of an additional lower retentivity phase in the form of high apparent diffusivity and substantially younger step ages (down to 40 Ma after Shallowater) in the initial ~3% of the extracted Xe (Fig. 4a, c). Although the diffusion kinetics of this phase is not absolutely quantified, its higher apparent diffusivity at lower temperatures suggests that this phase did not quantitatively retain  $^{129}\text{Xe}$  until at least ~40 Ma after Shallowater, and can be explained by a relatively low temperature event ( $\ll 390^\circ\text{C}$ ) or chemical alteration at that time or after. Note that the influence of this low retentivity phase does not strongly affect the 390°C constraint placed by the apparent plateau age (Fig. 4d).

It has been suggested that the Allende parent body experienced Sr isotopic redistribution as recently as  $4.36 \pm 0.08$  Ga ago (142), which may have involved elevated temperatures. If they were sufficiently high, elevated thermal conditions at that time would have caused observable diffusive loss of  $^{129}\text{Xe}^*$ . In addition to the 390°C thermal pulse shown in Fig. 4b, we modeled a subsequent thermal pulse at 4.36 Ga using the same diffusion kinetics as described above (i.e., Fig. 4a) to assess this possibility and constrain the permissible late-stage thermal conditions (Fig. S13). Because the Arrhenius plot bears evidence of an additional phase with higher diffusivity at low temperature, this calculation places an upper bound on the thermal conditions (Fig. S13c). If diffusivity of the additional phase is higher the thermal conditions constrained primarily by the first two steps would be even lower. Since  $^{129}\text{I}$  was effectively extinct by 4.36 Ga, this calculation also constrains the thermal conditions at all points in time after 4.36 Ga ago and the cumulative value of  $Dt/a^2$  resulting from multiple points in time. For these reasons the curve shown in Fig. S13c places a strong upper bound on the late-stage thermal conditions permitted by the Allende CAI T3 data, including any episodes of elemental redistribution within the past 2 Ga possibly recorded by open-system behaviour of the Re/Os systems of CAIs (143). Significant late-stage heating beyond this bound would have perturbed or eliminated the  $^{129}\text{Xe}/^{128}\text{Xe}^*$  plateau clearly observed at  $\sim +2.5$  Ma relative to Shallowater.

## References:

39. Kirschvink JL, Kopp RE, Raub TD (2008) Rapid, precise, and high-sensitivity acquisition of paleomagnetic and rock-magnetic data: Development of a low-noise automatic sample changing system for superconducting rock magnetometers. *Geochim. Geophys. Geosyst.* **9**:Q05Y01, doi:10.1029/2007GC001856.
40. Stephenson A (1983) Changes in the direction of the remanence of rocks produced by stationary alternating field demagnetization. *Geophys. J. R. Astr. Soc.* **73**:213-239.
41. Potter D, K., Stephenson A (1990) Field-impressed anisotropies of magnetic susceptibility and remanence in minerals. *J. Geophys. Res.* **95**:15573-11588.
42. Potter D, K., Stephenson A (1990) Field-impressed magnetic anisotropy in rocks. *Geophys. Res. Lett.* **17**:2437-2440.
43. Borradaile GJ, Lagroix F, Trimble D (2001) The effect of surface texture on the mineralogical analysis of chondritic meteorites using Raman spectroscopy. *Geophys. J. Int.* **147**:176-182.
44. Dankers PHM, Zijdeveld JDA (1981) Alternating field demagnetization of rocks and the problem of gyromagnetic remanence. *Earth Planet. Sci. Lett.* **53**:89-92.
45. Stephenson A (1993) Three-axis alternating field demagnetization of rocks and the identification of natural remanent magnetization, gyromagnetic magnetization, and anisotropy. *J. Geophys. Res.* **98**:373-381.
46. Garrick-Bethell I, Weiss BP, Shuster DL, Buz J (2009) Early lunar magnetism. *Science* **323**:356-359.
47. Fisher NI, Lewis T, Embleton BJJ (1987) *Statistical Analysis of Spherical Data* (Cambridge University Press, Cambridge).
48. Kirschvink JL (1980) The least-squares line and plane and the analysis of paleomagnetic data: examples from Siberia and Morocco. *Geophys. J. R. Astr. Soc.* **62**:699-718.
49. Gattacceca J, et al. (2008) On the efficiency of shock magnetization processes. *Phys. Earth Planet. Inter.* **166**:1-10.
50. Gattacceca J, et al. (2006) Investigating impact demagnetization through laser impacts and SQUID microscopy. *Geology* **34**:333-336.
51. Rochette P, et al. (2003) High pressure magnetic transition in pyrrhotite and impact demagnetization on Mars. *Geophys. Res. Lett.* **30**:1683.
52. Pearce CI, Patrick RAD, Vaughan DJ (2006) Electrical and magnetic properties of sulfides. *Rev. Mineral. Geochem.* **61**:127-180.
53. Rochette P, et al. (2005) Matching Martian crustal magnetization and magnetic properties of Martian meteorites. *Meteorit. Planet. Sci.* **40**:529-540.
54. Rochette P, et al. (2008) Magnetic classification of stony meteorites: 2. Non-ordinary chondrites. *Meteorit. Planet. Sci.* **43**:959-980.
55. Dunlop DJ, Özdemir O (1997) *Rock Magnetism: Fundamentals and Frontiers* (Cambridge University Press, New York).
56. Bennett CEG, Graham J (1980) New observations on natural pyrrhotites. Part III. Thermomagnetic experiments. *Am. Mineral.* **66**:1254-1257.
57. Schwarz EJ, Vaughan DJ (1972) Magnetic phase relations of pyrrhotite. *J. Geomag. Geoelectr.* **24**:441-458.
58. Bina M, Daly L (1994) Mineralogical change and self-reversed magnetizations in pyrrhotite resulting from partial oxidation; geophysical implications. *Phys. Earth Planet. Inter.* **85**:83-89.
59. Tsuchiyama A, et al. (2003) Three-dimensional structures of chondrules and their high-speed rotation. *Lunar Planet. Sci.* **34**:abstract #1271.
60. Weinbruch S, Armstrong J, Palme H (1994) Constraints on the thermal history of the Allende parent body as derived from olivine-spinel thermometry and Fe/Mg interdiffusion in olivine. *Geochim. Cosmochim. Acta* **58**:1019-1030.
61. Huss GR, Lewis RS (1994) Noble gases in presolar diamonds II: Component abundances reflect thermal processing. *Meteoritics* **29**:811-829.
62. Le Guillou C, Rouzaud JN, Findling N, Düber S (2009) Experimental graphitization and oxidation kinetic of nanodiamond: Implication for nebular for thermal processing. *Lunar Planet. Sci.* **40**:abstract #2070.
63. Cody GD, et al. (2008) Organic thermometry for chondritic parent bodies. *Earth Planet. Sci. Lett.* **272**:446-455.
64. Zolensky ME, Krot AN, Benedix G (2008) Record of low-temperature alteration in asteroids. *Rev. Mineral. Geochem.* **68**:429-462.

65. Clayton RS, et al. (1970) The Allende, Mexico, meteorite shower. *Smithsonian Contib. Earth. Sci.* **5**:1-53.
66. Fuchs LH, Olsen E (1973) Composition of metal in Type III carbonaceous chondrites and its relevance to the source-assignment of lunar metal. *Earth Planet. Sci. Lett.* **18**:379-384.
67. Herndon JM, Rowe MW, Larson EE, Watson DE (1976) Thermomagnetic analysis of meteorites, 3. C3 and C4 chondrites. *Earth Planet. Sci. Lett.* **29**:283-290.
68. Haggerty SE, McMahon BM (1979) Magnetite-sulfide-metal complexes in the Allende meteorite. *Proc. Lunar Planet. Sci. Conf. 10th*:851-870.
69. Miura Y, Smith DGW, Launspach S (1988) The Ni, Fe and Co contents of metal phases in the Allende, Holbrook and Nuevo Mercurio chondrites. *Mem. Natl. Inst. Polar Res.* **30**:224-235.
70. Bland PA, Cressey G, Menzies ON (2004) Modal mineralogy of carbonaceous chondrites by X-ray diffraction and Mossbauer spectroscopy. *Meteorit. Planet. Sci.* **39**:3-16.
71. Müller WF, Weinbruch S, Walter R, Müller-Beneke G (1995) Transmission electron microscopy of chondrule minerals in the Allende meteorite: Constraints on the thermal and deformational history of granular olivine-pyroxene chondrules. *Planet. Space Sci.* **43**:469-483.
72. Funaki M, Wasilewski P (2000) Pentlandite and magnetic anisotropy in Allende CV3 chondrite. *Lunar Planet. Sci.* **31**:abstract #1148.
73. Malissa H, Hermann F, Kluger F, Kiesel W (1972) Chemical and microprobe investigations of the Allende-meteorite. *Mikrochim Acta*:434-450.
74. Armstrong JT, El Goresy A, Wasserburg GJ (1985) Willy: A prize noble Ur-Fremdling-Its history and implications for the formation of Fremdlinge and CAI. *Geochim. Cosmochim. Acta* **49**:1001-1022.
75. Armstrong JT, Hutcheon ID, Wasserburg GJ (1987) Zeld and Company: Petrogenesis of sulfide-rich Fremdlinge and constraints on solar nebular processes. *Geochim. Cosmochim. Acta* **51**:3155-3173.
76. Fleet ME (2006) Phase equilibria at high temperatures. *Rev. Mineral. Geochem.* **61**:365-419.
77. Kontny A, De Wall H, Sharp TG, Posfai M (2000) Mineralogy and magnetic behavior of pyrrhotite from a 260 °C section at the KTB drilling site, Germany. *Am. Mineral.* **85**:1416-1427.
78. Day R, Fuller M, Schmidt VA (1977) Hysteresis properties of titanomagnetites: grain-size and compositional dependence. *Physics of The Earth and Planetary Interiors* **13**:260-267.
79. Dunlop DJ (2002) Theory and application of the Day plot (Mrs/Ms versus Hcr/Hc) - 1. Theoretical curves and tests using titanomagnetite data. *J. Geophys. Res.* **107**:doi:10.1029/2001JB000486.
80. Cisowski CS (1987) in *Geomagnetism*, ed. Jacobs JA (Academic Press, London), pp. 525-560.
81. Yang C-W, Williams DB (1996) A revision of the Fe Ni phase diagram low temperatures. *J. Phase Equilibria* **17**:522-531.
82. Cacciamani G, et al. (2006) Critical evaluation of the Fe-Ni, Fe-Ti, and Fe-Ni-Ti alloy systems. *Intermetallics* **14**:1312-1325.
83. Müller WF (1991) Microstructure of minerals in a chondrule from the Allende meteorite II. Thermal history deduced from clinopyroxenes and other minerals. *Neues Jahrbuch Miner. Abh* **162**:237-259.
84. Miura Y, Smith DGW, Launspach S (1983) The Ni, Fe and Co contents of metal phases in the Allende, Holbrook and Nuevo Mercurio chondrites. *Mem. Natl. Inst. Polar Res. Spec. Issue* **30**:Mem. Natl. Inst. Polar Res.
85. Liu H, et al. (1998) Structural and magnetic properties of (Fe<sub>1-x</sub>Co<sub>x</sub>)<sub>3</sub>P compounds: experiment and theory. *J. Magn. Magn. Mater.* **189**:69-82.
86. Shi L, Lianfang C, Yingting X (1988) Mössbauer study of the Ningqiang carbonaceous meteorites. *Hyperfine Interactions* **41**:815-817.
87. Oliver FW, Isuk EE, Wynter C (1984) Mössbauer study of the Allende meteorite. *Meteoritics* **19**:25-27.
88. Weselucha-Birczunski A, Zmudzka M (2008) Micro-Raman spectroscopy characterization of selected meteorites. *J. Mol. Struct.* **887**:253-261.
89. Burns RG (1993) in *Remote geochemical analysis: Elemental and mineralogical composition*, eds. Pieters CM & Englert PJ (Cambridge University Press, Cambridge), pp. 539-556.
90. Hoffman E, Seifu D, Oliver FW (2000) Axtell and Allende: A Mössbauer spectroscopic study. *Meteorit. Planet. Sci.* **35**:431-434.
91. Ozdemir O, Dunlop DJ (2002) Thermoremanence and stable memory of single-domain hematites. *Geophysical Research Letters* **29**:art. no.-1877.
92. Peters C, Dekkers MJ (2003) Selected room temperature magnetic parameters as a function of mineralogy, concentration and grain size. *Phys. Chem. Earth* **28**:659-667.
93. Rochette P, et al. (2009) Magnetic classification of stony meteorites: 3. Achondrites. *Meteorit. Planet. Sci.* **44**:405-427.
94. Brecher A, Arrhenius G (1974) The paleomagnetic record in carbonaceous chondrites: Natural remanence and magnetic properties. *J. Geophys. Res.* **79**:2081-2106.
95. Dekkers MJ (1988) Magnetic-properties of natural pyrrhotite I. Behavior of initial susceptibility and saturation-magnetization-related rock-magnetic parameters in a grain-size dependent framework. *Phys. Earth Planet. Inter.* **52**:376-393.
96. Halgedahl SL, Jarrard R (1995) Low-temperature behavior of single-domain through multidomain magnetite. *Earth Planet. Sci. Lett.* **130**:127-139.
97. Dekkers MJ (1989) Magnetic properties of natural goethite-I. Grain-size dependence of some low- and high-field related rockmagnetic parameters measured at room temperature. *Geophys. J.* **97**:323-340.
98. Weiss BP, et al. (2000) A low temperature transfer of ALH84001 from Mars to Earth. *Science* **290**:791-795.
99. Dunlop DJ, Ozdemir O, Clark DA, Schmidt PW (2000) Time-temperature relations for the remagnetization of pyrrhotite (Fe<sub>7</sub>S<sub>8</sub>) and their use in estimating paleotemperatures. *Earth Planet. Sci. Lett.* **176**:107-116.
100. Pullaiah G, Irving G, Buchan KL, Dunlop DJ (1975) Magnetization changes caused by burial and uplift. *Earth Planet. Sci. Lett.* **28**:133-143.
101. Dunlop DJ (1973) Theory of the magnetic viscosity of lunar and terrestrial rocks. *Rev. Geophys. Space Phys.* **11**:855-901.
102. Lowrie W, Kent DV (1978) Characteristics of VRM in Oceanic Basalts. *J. Geophys.* **44**:297-315.

103. Yu Y, Tauxe L (2006) Acquisition of viscous remanent magnetization. *Phys. Earth Planet. Inter.* **159**:32-42.
104. Guskova YG (1978) Magnetic-field estimates on the magnetization of carbonaceous chondrites. *Meteoritika* **37**:144-151.
105. Muxworthy AR, McClelland E (2000) Review of the low-temperature magnetic properties of magnetite from a rock magnetic perspective. *Geophys. J. Int.* **140**:101-114.
106. Ozdemir O, Dunlop DJ, Moskowitz BM (1993) The effect of oxidation on the Verwey transition in magnetite. *Geophys. Res. Lett.* **20**:1671-1674.
107. Dunlop DJ (2006) Inverse thermoremanent magnetization. *J. Geophys. Res.* **111**:B12S02, doi:10.1029/2006JB004572.
108. Dekkers MJ (1989) Magnetic-properties of natural pyrrhotite 2. High-temperature and low-temperature behavior of Jrs and TRM as a function of grain-size. *Phys. Earth Planet. Inter.* **57**:266-283.
109. Rochette P, Fillon G, Mattéi J-L, Dekkers MJ (1990) Magnetic transition at 30-34 Kelvin in pyrrhotite: insight into a widespread occurrence of this mineral in rocks. *Earth Planet. Sci. Lett.* **98**:319-328.
110. Moskowitz BM, Frankel RB, Bazylinski DA (1993) Rock magnetic criteria for the detection of biogenic magnetite. *Earth Planet. Sci. Lett.* **120**:283-300.
111. Kohout T, et al. (2007) Low-temperature magnetic properties of the Neuschwanstein EL6 meteorite. *Earth Planet. Sci. Lett.* **261**:143-151.
112. Nesvorný D, et al. (2007) Express delivery of fossil meteorites from the inner asteroid belt to Sweden *Icarus* **188**:400-413.
113. Scherer P, Schultz L (2000) Noble gas record, collisional history, and pairing of CV, CO, CK, and other carbonaceous chondrites. *Meteorit. Planet. Sci.* **35**:145-153.
114. Ben-Yosef E, et al. (2008) Application of copper slag in geomagnetic archaeointensity research. *J. Geophys. Res.* **113**:doi:10.1029/2007JB005235.
115. Tauxe L, Staudigel H (2004) Strength of the geomagnetic field in the Cretaceous Normal Superchron: New data from submarine basaltic glass of the Troodos Ophiolite. *Geochim. Geophys. Geosyst.* **5**:doi:10.1029/2003GC000635.
116. Yu Y, Tauxe L, Genevey A (2004) Toward an optimal geomagnetic field intensity determination technique. *Geochim. Geophys. Geosyst.* **5**:doi:10.1029/2003GC000630.
117. Ben-Yosef E, et al. (2008) A new approach for geomagnetic archaeointensity research: insights on ancient metallurgy in the Southern Levant. *J. Archaeol. Sci.* **35**:2863-2879.
118. Lawrence K, Johnson C, Tauxe L, Gee J (2008) Lunar paleointensity measurements: Implications for lunar magnetic evolution. *Phys. Earth Planet. Inter.*:doi:10.1016/j.pepi.2008.1005.1007.
119. Tauxe L, Banerjee SK, Butler RF, Van der Voo R (2009) *Essentials of Paleomagnetism* (University of California Press, Berkeley).
120. DePaolo DJ, Stolper EM, Thomas DM, Garcia MO (1999) (Pasadena).
121. Weiss BP, Lima EA, Fong LE, Baudenbacher FJ (2007) Paleointensity of the Earth's magnetic field using SQUID microscopy. *Earth Planet. Sci. Lett.* **264**:61-71.
122. Walton D (1987) Improving the accuracy of geomagnetic intensity measurements. *Nature* **328**:789-791.
123. Valet J-P, et al. (1996) Absolute paleointensity and magnetomineralogical changes. *J. Geophys. Res.* **101**:25,029-025,044.
124. McClelland E, Briden JC (1996) An improved methodology for Thellier-type paleointensity determination in igneous rocks and its usefulness for verifying primary thermoremanence. *J. Geophys. Res.* **101**:21,995-922,013.
125. Leonhardt R, Heunemann C, Krása D (2004) Analyzing absolute paleointensity determinations: Acceptance criteria and the software ThellierTool4.0. *Geochim. Geophys. Geosyst.*
126. Leonhardt R, Krása D, Coe RS (2004) Multidomain behavior during Thellier paleointensity experiments: a phenomenological model. *Phys. Earth Planet. Inter.* **147**:127-140.
127. Tauxe L, Love JJ (2003) Paleointensity in Hawaiian Scientific Drilling Project Hole (HSDP2): Results from submarine basaltic glass. *Geochim. Geophys. Geosyst.* **4**:8702, doi:10.1029/2001GC000276.
128. Coe RS, et al. (2004) Multidomain behavior during Thellier paleointensity experiments: results from the 1915 Mt. Lassen flow. *Phys. Earth Planet. Inter.* **147**:141-153.
129. Halgedahl SL, Day SR, Fuller M (1980) The effect of cooling rate on the intensity of weak-field TRM in single-domain magnetite. *J. Geophys. Res.* **95**:3690-3698.
130. Dunlop DJ, Argyle KS (1997) Thermoremanence, anhysteretic remanence, and susceptibility of submicron magnetites: Nonlinear field dependence and variation in grain size. *J. Geophys. Res.* **102**:20199-20210.
131. Fabian K (2009) Thermochemical remanence acquisition in single-domain particle ensembles: A case for possible overestimation of the geomagnetic paleointensity. *Geochim. Geophys. Geosyst.* **10**:doi:10.1029/2009GC002420.
132. Bouvier A, et al. (2007) Pb-Pb dating constraints on the accretion and cooling history of chondrites. *Geochim. Cosmochim. Acta* **71**:1583-1604.
133. MacPherson GJ, Davis AM, Zinner EK (1995) The distribution of aluminum-26 in the early solar system - A reappraisal. *Meteoritics* **30**:365-386.
134. LaTourrette T, Wasserburg GJ (1998) Mg diffusion in anorthite: Implications for the formation of early solar system planetesimals. *Earth Planet. Sci. Lett.* **158**:91-108.
135. Amelin Y, Krot AN (2007) Pb isotopic age of the Allende chondrules. *Meteorit. Planet. Sci.* **42**:1321-1335.
136. Hutcheon ID, et al. (1998) <sup>53</sup>Mn-<sup>53</sup>Cr dating of fayalite formation in CV3 chondrite Mokoia: Evidence for asteroidal alteration. *Science* **282**:1865-1867.
137. Jessberger EK, Dominik B, Staudacher T, Herzog GF (1980) <sup>40</sup>Ar-<sup>39</sup>Ar ages of Allende. *Icarus* **42**:380-405.
138. Villa IM, Huneke JC, Wasserburg GJ (1983) <sup>39</sup>Ar recoil losses and presolar ages in Allende inclusions. *Earth Planet. Sci. Lett.* **63**:1-12.
139. Jessberger EK (1984) <sup>39</sup>Ar recoil and the apparent persistence of the presolar age of an Allende inclusion. *Earth Planet. Sci. Lett.* **69**:1-12.
140. Herzog GF, et al. (1980) <sup>39</sup>Ar/<sup>40</sup>Ar systematics of Allende inclusions. *Proc. Lunar Planet. Sci. Conf. 11th*:959-976.
141. Eugster O, Lorenzetti S, Krahenbuhl U, Marti K (2007) Comparison of cosmic-ray exposure ages and trapped noble gases in chondrule and matrix samples of ordinary,



- enstatite, and carbonaceous chondrites. *Meteorit. Planet. Sci.* **42**:1351-1371.
142. Shimoda G, et al. (2005) Evidence from the Rb-Sr system for 4.4 Ga alteration of chondrules in the Allende (CV3) parent body. *Meteorit. Planet. Sci.* **40**:1059-1072.
  143. Becker H, et al. (2001) Rhenium-osmium systematics of calcium-aluminium-rich inclusions in carbonaceous chondrites. *Geochim. Cosmochim. Acta* **65**:3379-3390.
  144. Fireman EL, DeFelice J, Norton E (1970) Ages of the Allende meteorite. *Geochim. Cosmochim. Acta* **34**:873-881.
  145. Gilmour JD, Crowther SA, Busfield A, Holland G, Whitby JA (2009) An early I-Xe age for the CB chondrite chondrule formation, and a re-evaluation of the closure age of Shallowater enstatite. *Meteorit. Planet. Sci.* **44**:573-579.
  146. Hohenberg CM, Pravdivtseva OV (2008) I-Xe dating: From adolescence to maturity. *Chemie der Erde* **68**:339-351.
  147. Swindle TD (1998) Implications of iodine-xenon studies for the timing and location of secondary alteration. *Meteorit. Planet. Sci.* **33**:1147-1155.
  148. Zaikowski A (1980) I-Xe dating of Allende inclusions: Antiquity and fine structure. *Earth Planet. Sci. Lett.* **47**:211-222.
  149. Swindle TD, Caffee MW, Hohenberg CM, Lindstrom MM (1983) I-Xe studies of individual Allende chondrules. *Geochim. Cosmochim. Acta* **47**:2157-2177.
  150. Kirschbaum C (1988) Carrier phases for iodine in the Allende meteorite and their associated Xe-129(R)/I-127 ratios - a laser microprobe study. *Geochim. Cosmochim. Acta* **52**:679-699.
  151. Pravdivtseva OV, et al. (2003) The I-Xe record of alteration in the Allende CV chondrite. *Geochim. Cosmochim. Acta* **67**:5011-5026.
  152. Lavielle B, Marti K (1992) Trapped xenon in ordinary chondrites. *J. Geophys. Res.* **97**:20875-20881.
  153. Fechtig H, Kalbitzer ST (1966) in *Potassium Argon Dating*, eds. Schaeffer OA & Zähringer J (Springer-Verlag, New York), pp. 68-107.